Geophysical Journal International

Geophys. J. Int. (2015) **201,** 90–111 doi: 10.1093/gji/ggu472

GJI Seismology

3-D numerical simulations of earthquake ground motion in sedimentary basins: testing accuracy through stringent models

Emmanuel Chaljub,[1] Emeline Maufroy,[1] Peter Moczo,[2,3] Jozef Kristek,[2,3] Fabrice Hollender,[1,4] Pierre-Yves Bard,[1] Enrico Priolo,[5] Peter Klin,[5] Florent de Martin,[6] Zhenguo Zhang,[7] Wei Zhang[7] and Xiaofei Chen[7]

[1] *Univ. Grenoble Alpes/CNRS/IRD/IFSTTAR, ISTerre, F-38000 Grenoble, France. E-mail: Emmanuel.Chaljub@obs.ujf-grenoble.fr*
[2] *Faculty of Mathematics, Physics and Informatics, Comenius University Bratislava, Mlynska dolina F1, 84248 Bratislava, Slovak Republic*
[3] *Geophysical Institute, Slovak Academy of Sciences, Dubravska cesta 9, 84528 Bratislava, Slovak Republic*
[4] *French Alternative Energies and Atomic Energy Commission (CEA), Saint-Paul-lez-Durance, France*
[5] *Istituto Nazionale di Oceanografia e Geofisica Sperimentale, Trieste, Italy*
[6] *Bureau de Recherches Géologiques et Minières, Risks and Prevision Division, 3 avenue C. Guillemin, BP 36009, F-45060 Orléans Cedex 2, France*
[7] *School of Earth and Space Sciences, University of Science and Technology of China, Hefei, Anhui 230026, China*

Accepted 2014 December 4. Received 2014 December 1; in original form 2014 July 10

SUMMARY

Differences between 3-D numerical predictions of earthquake ground motion in the Mygdonian basin near Thessaloniki, Greece, led us to define four canonical stringent models derived from the complex realistic 3-D model of the Mygdonian basin. Sediments atop an elastic bedrock are modelled in the 1D-sharp and 1D-smooth models using three homogeneous layers and smooth velocity distribution, respectively. The 2D-sharp and 2D-smooth models are extensions of the 1-D models to an asymmetric sedimentary valley. In all cases, 3-D wavefields include strongly dispersive surface waves in the sediments. We compared simulations by the Fourier pseudo-spectral method (FPSM), the Legendre spectral-element method (SEM) and two formulations of the finite-difference method (FDM-S and FDM-C) up to 4 Hz.

The accuracy of individual solutions and level of agreement between solutions vary with type of seismic waves and depend on the smoothness of the velocity model. The level of accuracy is high for the body waves in all solutions. However, it strongly depends on the discrete representation of the material interfaces (at which material parameters change discontinuously) for the surface waves in the sharp models.

An improper discrete representation of the interfaces can cause inaccurate numerical modelling of surface waves. For all the numerical methods considered, except SEM with mesh of elements following the interfaces, a proper implementation of interfaces requires definition of an effective medium consistent with the interface boundary conditions. An orthorhombic effective medium is shown to significantly improve accuracy and preserve the computational efficiency of modelling.

The conclusions drawn from the analysis of the results of the canonical cases greatly help to explain differences between numerical predictions of ground motion in realistic models of the Mygdonian basin.

We recommend that any numerical method and code that is intended for numerical prediction of earthquake ground motion should be verified through stringent models that would make it possible to test the most important aspects of accuracy.

Key words: Numerical solutions; Numerical approximations and analysis; Earthquake ground motions; Site effects; Computational seismology; Wave propagation.

1 INTRODUCTION

Seismologists must predict earthquake ground motion during potential future earthquakes in densely populated areas and sites of special importance. This is very important for land-use planning, designing new buildings and reinforcing existing ones. It is also very important for undertaking actions that could help mitigate losses during future earthquakes.

Prediction of the earthquake ground motion for a site of interest can be based on empirical approach if sufficient earthquake records at that site or at a sufficiently similar site are available. In most cases, however, this is not so and seismologists face a drastic lack of data. In such situations it is the theory and numerical simulations that have to be applied for predicting the earthquake motion.

Structural and rheological complexity of the realistic models imply that only approximate computational methods can be applied. Among the approximate methods, the domain (in the spatial sense) numerical-modelling methods are dominant due to relatively reasonable balance between the accuracy and computational efficiency. Some of the more widely used numerical-modelling methods are the time-domain finite-difference, finite-element, Fourier pseudo-spectral, spectral-element and discontinuous Galerkin methods.

Each method has its advantages and disadvantages that often depend on a particular application. In other words, none of these methods can be chosen as the universally best (in terms of accuracy and computational efficiency) method for all important problems. One logical consequence and particular aspect of this situation is that, depending on a particular model of the medium, it might be not trivial to reach satisfactory agreement between solutions obtained by different methods. And indeed, this is the important lesson learned from the dedicated international blind predictions tests and comparative exercises for the Turkey Flat in the Parkfield area, central California in 1989–1990 (e.g. Cramer 1995), Ashigara Valley in the Kanagawa Prefecture, SW of Tokyo, Japan in 1992 (e.g. Bard 1994), Osaka basin, Japan in 1998 (Kawase & Iwata 1998), Grenoble valley in French Alps in 2006 (Chaljub *et al.* 2006, 2010) as well as from the Southern California Earthquake Center (SCEC) code comparison (Day *et al.* 2001, 2003, 2005; Bielak *et al.* 2010).

The SCEC comparison included relatively simple models of a homogeneous half-space and layer over half-space (Day *et al.* 2001), and a realistic model of the San Fernando Valley and Los Angeles Basin (Day *et al.* 2003, 2005). In the simple models the *P*- to *S*-wave velocity ratio was as low as 1.73 and the *S*-wave velocity contrast less than 1.5. Due to the material parameters and source position, strong surface waves were not generated in the models. Bielak *et al.* (2010) analysed results of verification for the ShakeOut scenario earthquake for the realistic SCEC community velocity model and frequency range [0.1, 0.5] Hz. They concluded that the independent simulations were, given the complexity and size of the problem, satisfactorily close. They attributed the observed differences mainly to differences in discrete representations of the model heterogeneity and models of attenuation.

The ESG2006 (Effects of Surface Geology 2006) exercise was focused on the Grenoble valley in the French Alps (Chaljub *et al.* 2006, 2010). Compared with the Los Angeles basin, the modelling of the Grenoble Valley is complicated by the larger *P*- to *S*-wave velocity ratio, larger velocity contrast and the complex interface geometry. The simulations were performed for the frequency range [0.1, 2] Hz. Four teams reached a very good level of agreement up to 1 Hz. The differences above 1 Hz were attributed to differences in discrete representations of the model heterogeneity, numerical dispersion and models of attenuation, that is, similar to reasons found by Bielak *et al.* (2010).

The individual named reasons for differences in both comparisons for realistic models are probably correct but they were not really separated and quantified. In other words, none of the three comparisons (SCEC simple models, SCEC ShakeOut and ESG2006) provides sufficient methodological basis for estimating accuracy of individual numerical solutions and possible differences among independent numerical solutions for relatively simple but stringent models or for other complex realistic models. This, however, is an important aspect in relation to application of the numerical-modelling methods in practical predictions.

Given the state-of-the-art in the numerical modelling of earthquake motion it was logical to develop a project focused on systematic and quantitative comparison of the most advanced numerical methods. The Aristotle University of Thessaloniki, Greece, the Cashima research project (supported by CEA—the French Alternative Energies and Atomic Energy Commission, and the Laue-Langevin Institute, ILL, Grenoble) and ISTerre at Joseph Fourier University, Grenoble, France, jointly organized the Euroseistest Verification and Validation Project (E2VP) which aims at: (i) evaluating accuracy of the current most advanced numerical methods when applied to realistic 3-D models and (ii) quantitative comparison of the recorded and numerically simulated earthquake ground motion. E2VP thus includes both verification and validation (e.g. Bielak *et al.* 2010; Moczo *et al.* 2014). The E2VP target site is the Mygdonian basin near Thessaloniki, Greece, the international research and test site of many international seismological and earthquake-engineering projects (for more on the site see Maufroy *et al.* 2014).

In this paper, we address the verification part of E2VP. From the originally 18 teams from around the world intended to participate, eight teams contributed to the 3-D modelling over the whole duration of the first verification phase and four teams were able to reach a satisfactory level of agreement for the complex 3-D models of the Mygdonian basin [one team applied its finite-difference scheme, one team Fourier pseudo-spectral scheme and two teams independent implementations of the spectral-element method (SEM)].

Importantly and consistently with the previous comparative efforts mentioned above, there were differences among individual solutions by the four teams mainly in the configurations with strong surface waves and at high frequencies—despite the effort to make the individual discrete models as close as possible. The differences led us to develop 4 canonical models derived from the realistic 3-D model of the Mygdonian basin. Two models are 1-D, two models are 2-D. Wavefields are in the all models 3-D. The solutions for the canonical models were computed by the four original teams and by a fifth team which applied the velocity–stress collocated-grid finite-difference scheme.

The quantitative analysis of the results explains how the accuracy of individual solutions and level of agreement between solutions vary with the type of seismic waves and depend on the discretization of the spatial variations of material parameters.

2 EUROSEISTEST VERIFICATION AND VALIDATION PROJECT

The target site of E2VP is the Mygdonian basin located in the northeastern part of Greece, 30 km ENE from Thessaloniki, in the epicentral area of the *M*6.4 seismic event which occurred on 1978 June 20 (e.g. Soufleris *et al.* 1982; Theodulidis *et al.* 2006). E2VP focuses on the part of the basin between the Lagada and Volvi lakes, a site which has been extensively investigated in several European projects (e.g. Euroseistest, Euroseismod, Euroseisrisk, ISMOD, ITSAK-GR; see `http://euroseisdb.civil.auth.gr`, last accessed 16 January 2015) and monitored with a dense accelerometric array since the mid-nineties. The project makes use of a detailed 3-D model of the intralake basin zone (about 5 km wide and 15 km long) based upon work by Manakou (2007) and Manakou *et al.* (2010). The model consists of three sedimentary layers with significant lateral variations in thickness as shown in

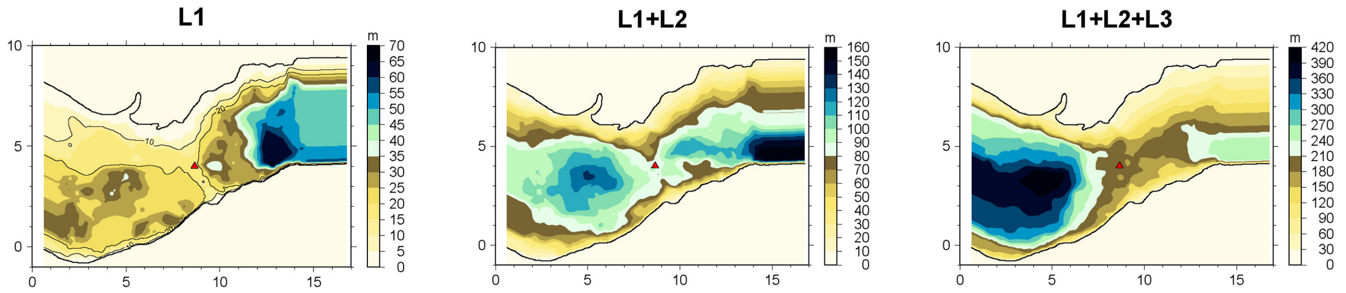

Figure 1. Thicknesses of the sedimentary layers of the Mygdonian basin's velocity model used within the E2VP project. The red triangle denotes the position of TST, the central station of the Euroseistest accelerometric array.

Table 1. Thicknesses (h) and material parameters (S and P seismic velocities V_S and V_P, respectively, and mass density ρ) in the model with three homogeneous layers used in E2VP. L_i, $i = 1\ldots3$ denote the sedimentary layers and H the surrounding bedrock.

	h (m)	V_P (m s^{-1})	V_S (m s^{-1})	ρ (kg m^{-3})
L_1	17.3	1500	200	2100
L_2	72.5	1800	350	2100
L_3	115.6	2500	650	2200
H	1000	4500	2600	2600

Table 2. Same as Table 1 for the smooth, piecewise linear, three-layer model used in E2VP.

	h (m)	V_P (m s^{-1})	V_S (m s^{-1})	ρ (kg m^{-3})
L_1	17.3	[1500–1600]	[200–250]	2100
L_2	72.5	[1600–2200]	[250–500]	[2100–2130]
L_3	115.6	[2200–2800]	[500–900]	[2130–2250]
H	1000	4500	2600	2600

Fig. 1. Note that the TST station at the centre of the Euroseistest site is located at a saddle point, with the sedimentary thickness increasing both eastward and westward, and decreasing towards the edges of the basin. The central NS profile passing through TST appears as a buried pass between two thicker sub-basins, the maximum thickness (about 400 m) being reached in the westernmost one. Based upon this three-layer structure of the basin, two different velocity models have been considered in E2VP: a piecewise homogeneous model with physical interfaces within the sediments, and a smooth, piecewise linear model without internal discontinuities. The depth distribution of seismic velocities and mass densities in each sedimentary layer and in the surrounding bedrock is given for both models in Tables 1 and 2, respectively. The intrinsic attenuation is modelled through a linear scaling of the quality factor with shear wave velocity as $Q_S = V_S/10$, neglecting the bulk attenuation, $Q_\kappa = \infty$.

Many different numerical methods were compared during the verification phase of E2VP, to evaluate the epistemic uncertainty in numerical prediction of earthquake ground motion in sedimentary basins. Here we consider a subset of those methods which provided the most similar results: the velocity–stress finite-difference method on the staggered grid (FDM-S), the Fourier pseudo-spectral method (FPSM) and the Legendre SEM. They are are briefly described in Section 4. The reader is referred to Maufroy *et al.* (2014) for a presentation of the results obtained by a wider set of methods and codes, which allows to better appreciate the difficulty to obtain acceptable levels of agreement in realistic 3-D verification exercises.

In Fig. 2, we compare synthetics simulated at the TST station by the three methods for frequencies up to 4 Hz for the viscoelastic model with three homogeneous layers. The basin is excited by a double-couple point source located at 3 km depth. The level of similarity is excellent for the first arrivals (i.e. for $t \leq 5$ s), which consist mainly of body waves, and it decreases for late arrivals consisting mostly of surface waves diffracted at the basin edges. In Fig. 3, we compare synthetics for the elastic model with homogeneous layers. The neglect of attenuation reveals significant differences in amplitude and phase in the time window dominated by the local surface waves, that is for $t \geq 6$ s. Note that those differences remain even after increasing the grid resolution used in each of the numerical

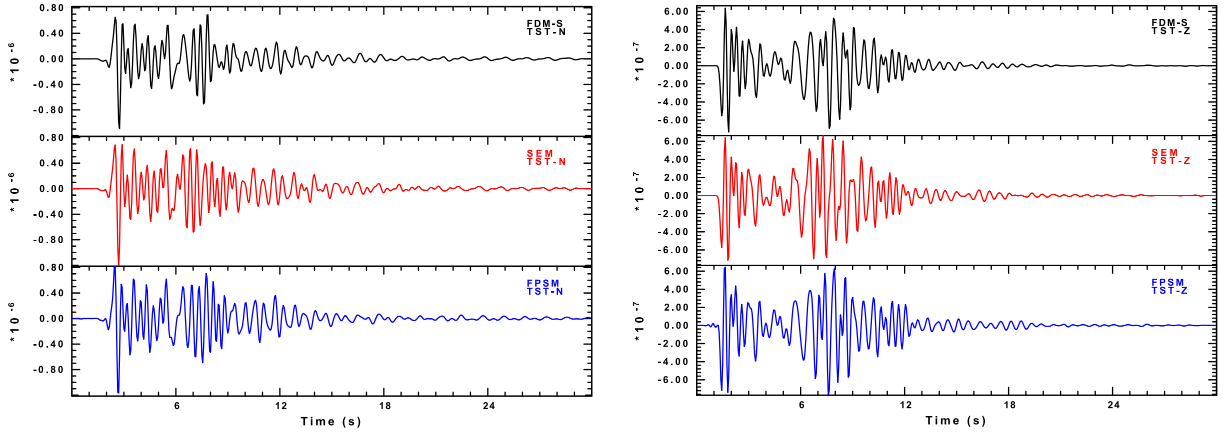

Figure 2. Comparison of predictions of the NS (left-hand panel) and vertical (right-hand panel) components of ground velocity at the central TST station obtained by three different numerical methods: FDM-S (black), SEM (red) and FPSM (blue). The sedimentary basin is modelled with three homogeneous viscoelastic layers of varying thicknesses described in Fig. 1 and Table 1.

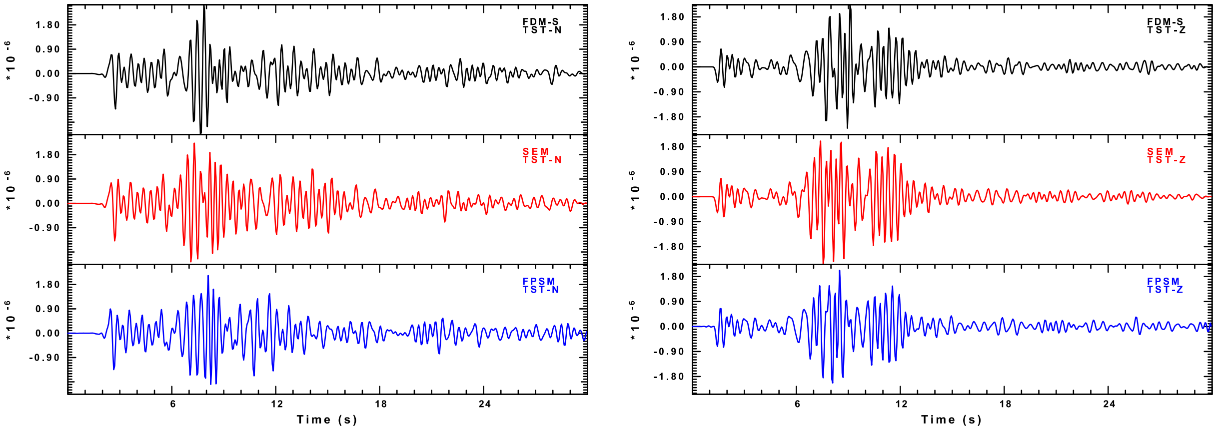

Figure 3. Same as Fig. 2 for the elastic model (neglecting intrinsic attenuation) with homogeneous layers. Note the good agreement on the first arrivals and the differences in phase and amplitude for later arrivals (between $t = 6$ and 12 s).

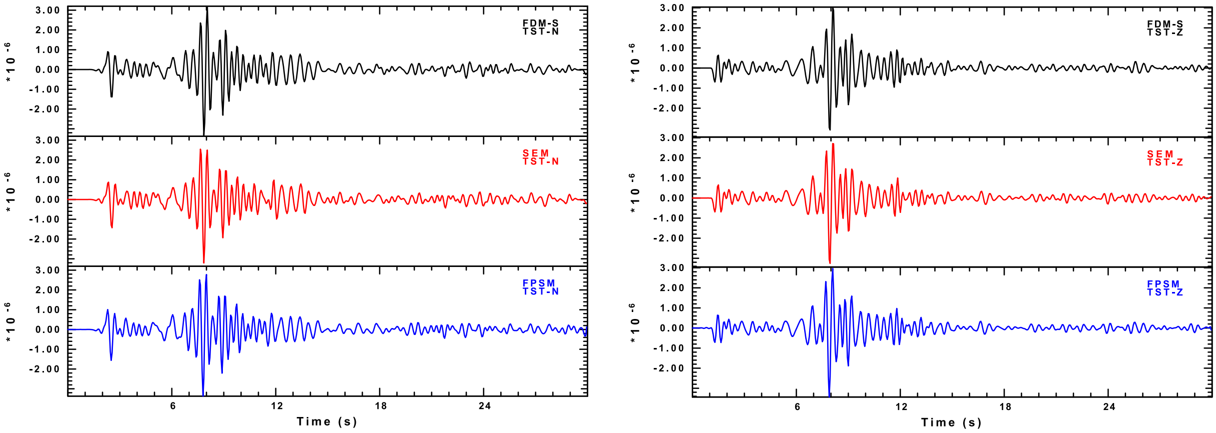

Figure 4. Same as Fig. 3 for the smooth basin model of Table 2: no internal material discontinuities in sediments. Note the overall good agreement obtained, even on late arrivals.

solutions. These results suggest that the epistemic uncertainty of numerical prediction of earthquake ground motion may be large for local surface waves. Several factors may contribute to this. They are investigated and discussed later in the paper.

Another important observation is that the level of epistemic uncertainty on the late arrivals was found smaller whenever a smooth basin model was considered. This is illustrated in Fig. 4 where we compare the predictions of the elastic response of the smooth piecewise linear model of Table 2. Despite the neglect of attenuation, the level of fit is excellent on the whole wavefield.

3 CANONICAL TEST CASES

In order to better understand the origin of the differences between numerical predictions of ground motion observed in the course of E2VP, we designed a set of test cases with relevant characteristics.

We focus on the perfectly elastic models because we checked that the differences between individual solutions were much larger when attenuation was neglected. The verification of solutions in the viscoelastic models is left for a further, second level analysis. We may note that reaching a satisfactory level of agreement in the elastic models represents a real numerical challenge.

In this paper, we present four test cases: two for which the velocity model is varying only in the vertical direction (1-D geometry), and two for which the velocity model is a simplified, 2-D cross-section of the Mygdonian basin model (2-D geometry). For each geometry (1-D or 2-D), two kinds of structural models were considered: one model, referred to as sharp, with internal discontinuities of the material parameters in the sedimentary part; and one model, referred to as smooth, where the vertical variation of the material parameters is continuous, piecewise linear within the sediments. The four test cases are denoted as 1D-sharp, 1D-smooth, 2D-sharp and 2D-smooth. The 3-D seismic wavefields include surface waves trapped in the sediments: for models with 1-D geometry, the surface waves are excited by a surface force, whereas they are spontaneously generated from the conversion of body waves at the basin edges for models with 2-D geometry.

3.1 Models with 1-D geometry

The problem configuration for the test cases with 1-D geometry (1D-sharp and 1D-smooth) is depicted in Fig. 5. The model consists of three sedimentary layers overlying an elastic, homogeneous halfspace. The layer thicknesses, densities and seismic velocities for the 1D-sharp and 1D-smooth models are given in Tables 1 and 2, respectively. The total sediment thickness is 205.4 m and the fundamental resonance frequencies are $f_0 \simeq 0.67$ and $\simeq$0.74 Hz for the 1D-sharp and 1D-smooth models, respectively. Note that although the 1D-smooth model was not designed to be a smooth approximation of the 1D-sharp model, whence the difference in the fundamental frequency, both models are consistent with the geological and geophysical information gathered at the TST site.

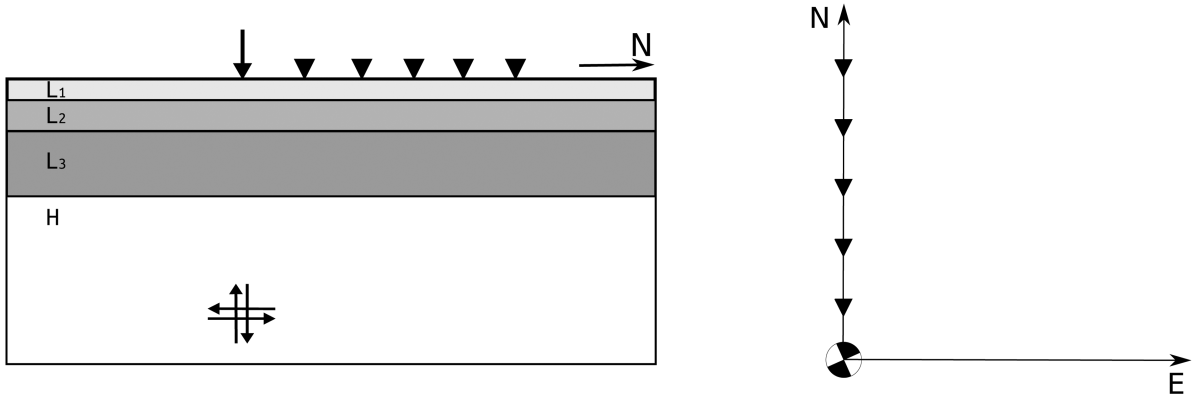

Figure 5. Schematic representation (left: vertical cross-section, right: surface view) of the 3 layers (L_1, L_2, L_3) over half-space (H) models used in the test cases 1D-sharp and 1D-smooth. The values of thicknesses, densities and seismic velocities are given in Tables 1 and 2. The positions of the sources and surface receivers are indicated with bold arrows and triangles, respectively. The beach ball at the epicentre indicates the focal mechanism of the double-couple point source plotted. The distance between the receivers along the northern surface profile is 1 km.

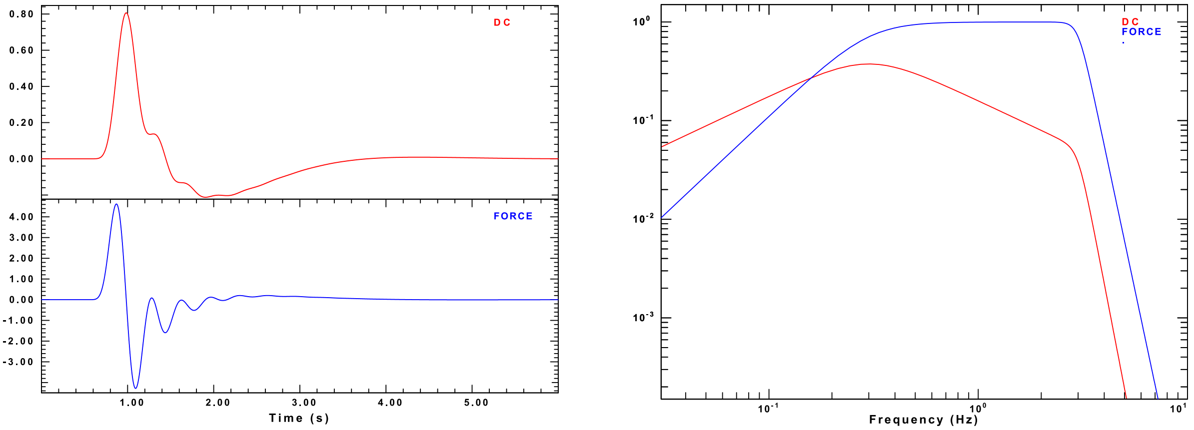

Figure 6. Source time functions used in the test cases 1D-sharp and 1D-smooth. Left-hand panel: dimensionless time histories for the deep double-couple source (red) and the surface force (blue). Right-hand panel: corresponding amplitude Fourier spectra.

The impact of the strategy used for constructing a geophysical model on the level of epistemic uncertainty in the numerical prediction of earthquake ground motion is discussed at the end of the paper.

A double-couple point source with strike ϕ_S, dip δ_S and rake λ_S is set at 3 km depth. The focal mechanism is that of a vertical strike-slip fault ($\delta_S = 90^\circ$, $\lambda_S = 0^\circ$), rotated such that the horizontal coordinate axes do not lie in any nodal plane of the radiation patterns for the P or S waves: $\phi_S = 22.5^\circ$. An additional vertical force is considered at the free surface in order to excite Rayleigh surface waves trapped in the sedimentary layers. Both sources act synchronously with the time functions shown in Fig. 6. The source time function for the surface force is a bandpass filtered Dirac pulse with almost no spectral content beyond $f_{\max} = 4$ Hz and a flat part in the band [0.3–3 Hz]; its integral is used to define the time history of the double-couple source. The seismic moment of the double-couple source is set to $M_0 = 10^{18}$ N.m and the amplitude of the surface force is multiplied by a factor $A = 5 \times 10^{11}$ in order to obtain synthetic seismograms with realistic ratios of body- to surface wave amplitudes.

3.1.1 Reference solutions

The reference solutions for the 1D-sharp and 1D-smooth cases were computed with the discrete wavenumber method (DWM; Bouchon 1981, 2003): we used the `axitra` program (Coutant 1989) to compute the wavefield generated by the deep double-couple source and a code implementing Hisada's asymptotic approximation at high wavenumbers (Hisada 1995) to compute the wavefield generated by the surface force.

Fig. 7 shows the synthetic seismograms computed at a few receivers located at the surface along the northern profile for the 1D-sharp case. The east–west component of ground velocity consists only of *SH* body waves and shows a typical 1-D resonance pattern at about 2.7 Hz, whereas the vertical component is dominated by the propagation of strongly dispersed Rayleigh surface waves. The time-frequency representation of the vertical ground velocity at 4 km epicentral distance is shown in Fig. 8. It helps to identify the contributions of the different Rayleigh modes to the 15 s long wave train recorded after 10 s: seismic phases arriving between 12 and 16 s consist mainly of the high-frequency (≥ 2 Hz) first higher mode, whereas phases arriving after 18 s are made of the moderate- to low-frequency fundamental mode ($\lesssim 3$ Hz). Note the large amplitude related to the arrival of the Airy phase of the fundamental Rayleigh mode around 17 s, which is well predicted by the analysis of the group velocity.

The surface seismograms for the 1D-smooth case are shown in Fig. 9. Note that, compared to the 1D-sharp case, the high-frequency resonance effect is less pronounced in the body wave part and that a simpler surface wave dispersion pattern is observed on the vertical component. Looking at the time-frequency representation of the vertical ground velocity at 4 km epicentral distance (Fig. 10), one

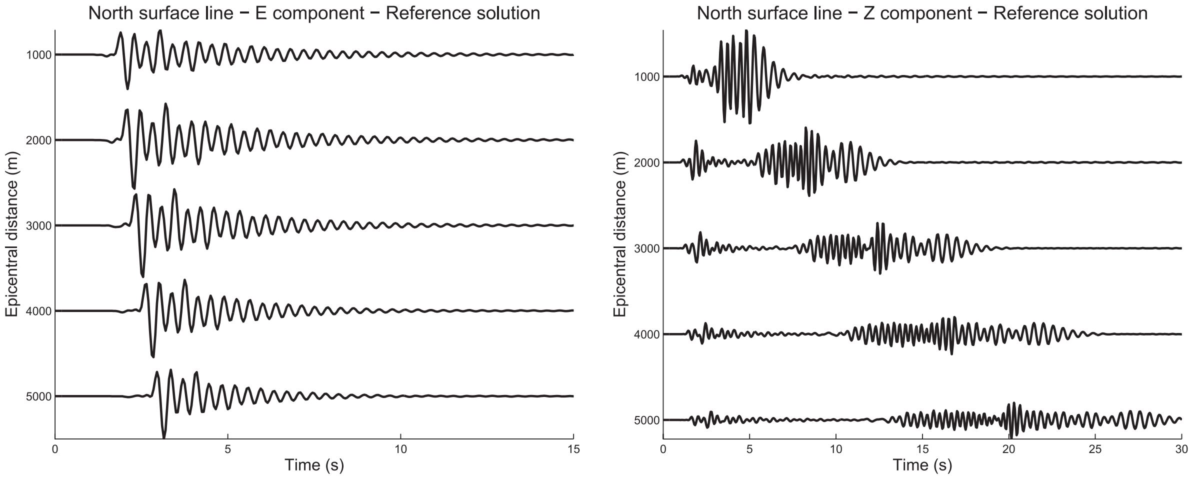

Figure 7. East–west (left-hand panel) and vertical (right-hand panel) components of ground velocity along the northern surface profile computed with the discrete wavenumber method for the 1D-sharp model.

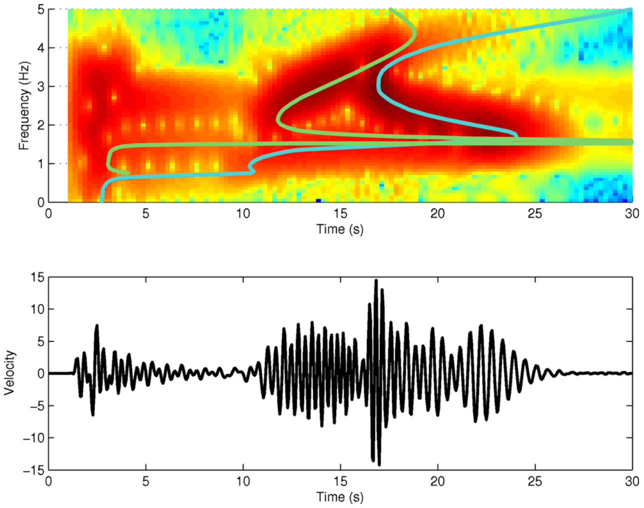

Figure 8. Time (bottom panel) and time-frequency (top panel) representations of the vertical ground velocity at 4 km epicentral distance for the 1D-sharp case. The background colours on the top image indicate the amplitude of the seismic arrivals, from blue (small) to red (medium) and bordeaux (large). The solid lines superimposed on the image indicate the theoretical group arrival times of the fundamental (blue) and first higher (green) modes of Rayleigh waves.

sees indeed that the fundamental and first higher modes of Rayleigh waves are well separated in time, the fundamental mode being much less dispersed than in the 1D-sharp case.

3.2 Models with 2-D geometry

The problem configuration for the test cases with 2-D geometry (2D-sharp and 2D-smooth) is shown in Fig. 11. The model corresponds to a 5-km-long valley bounded at one side by a vertical wall and at the other side by a gentle slope, in order to mimic the geometry of the north–south cross-section of the Mygdonian basin passing through the central TST station (Fig. 1). The layering for the 2D-sharp (resp. 2D-smooth) model is the same as that for the 1D-sharp (resp. 1D-smooth) model, except close to the northern edge where the thickness of each layer linearly decreases from its value given in Table 1 (resp. Table 2) to zero over a distance of 1.5 km. The resulting angle of the bedrock-sediment interface at the northern boundary is about 8°.

Both 2-D models are excited by the same deep double-couple source used for the 1D-sharp and 1D-smooth cases. In these models, contrary to the 1-D models, the surface waves (of Rayleigh and Love type) are generated at the edges of the valley and trapped in the sediments.

4 NUMERICAL METHODS

The numerical solutions presented in this paper were obtained by three kinds of numerical approximation in space: two velocity–stress formulations of the finite-difference method – on the staggered grid and on the collocated grid, the FPSM and the Legendre SEM. Time evolution in all cases is solved by an explicit, conditionally stable, finite-difference scheme. In what follows, we briefly present each method and explain how it should be implemented to provide an accurate solution to the canonical cases.

4.1 Legendre SEM

The SEM is a high-order finite-element approximation in which the consistent choice of an orthogonal polynomial basis and of a Gauss numerical quadrature allows to achieve the convergence properties of spectral methods. In its early applications to seismology (Priolo *et al.* 1994; Seriani & Priolo 1994), a set of Chebyshev polynomials and Gauss–Chebyshev quadrature were used. Using instead Legendre polynomials and Gauss–Legendre–Lobatto quadrature yields SEM, which still holds the convergence rate of spectral methods while providing a diagonal mass matrix resulting in costless implementation of explicit finite-difference schemes in time. The Legendre formulation of the SEM was introduced in seismology by Faccioli *et al.* (1997) and Komatitsch & Vilotte (1998), and is the most widely used nowadays. It relies on the tensorization of the 1-D SEM, and therefore on the use of quadrangles in 2-D and hexahedras in 3-D. The reader is referred to Komatitsch *et al.* (2005) and Chaljub *et al.* (2007) for review articles presenting the numerous developments of SEM, and to Moczo *et al.* (2014, chapter 5, p. 76) for a historical presentation and recent applications to seismic wave propagation in sedimentary basins or alluvial valleys.

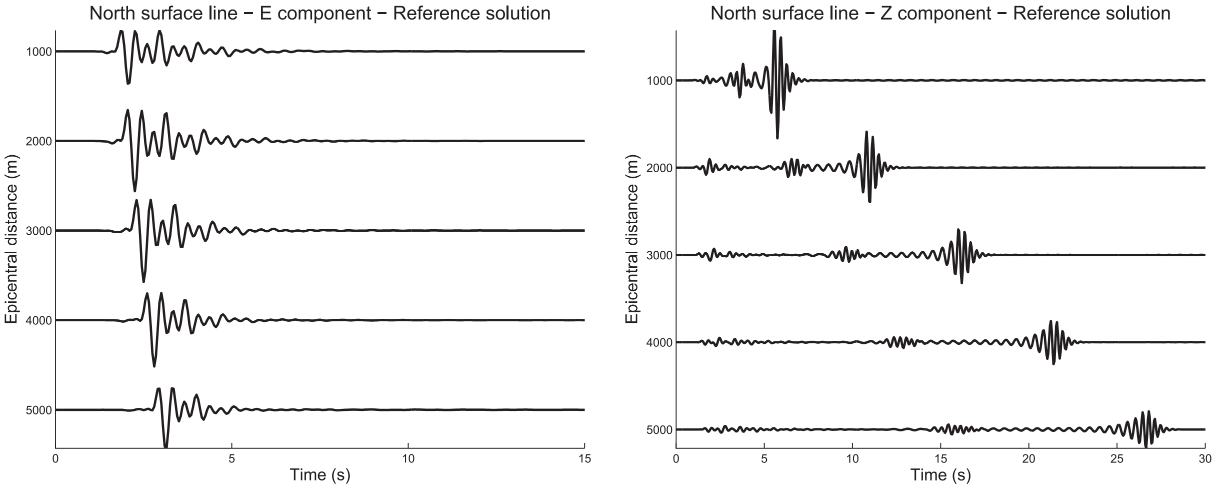

Figure 9. East–west (left-hand panel) and vertical (right-hand panel) components of ground velocity along the northern surface profile computed with the discrete wavenumber method for the 1D-smooth model.

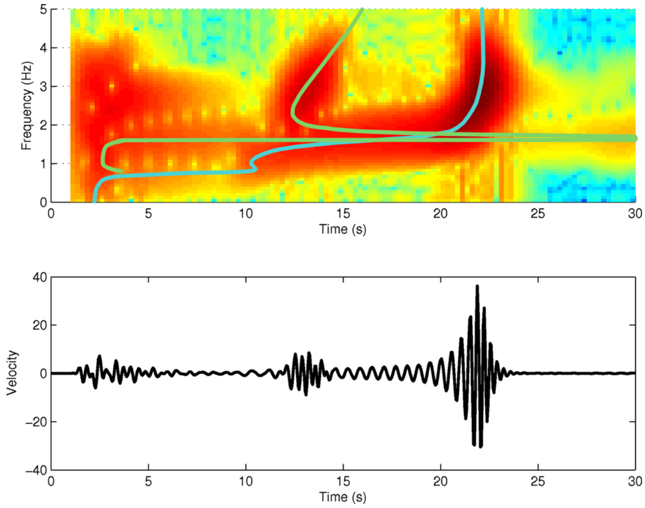

Figure 10. Same as Fig. 8 for the 1D-smooth case.

In the finite-element method (FEM), and therefore in SEM, the free-surface condition (and more generally the continuity of traction) is said to be a natural boundary condition because it is accounted for in the weak form of the equations to be solved and does not have to be explicitly enforced at the discrete level. This allows surface topography to be accounted for in SEM, as long as the variations of the free surface can be accurately represented at the discrete level. No particular effort, or care, was therefore needed when implementing the free-surface condition in SEM for the canonical cases considered here, since they all deal with a flat free surface.

Two kinds of material heterogeneities can be accounted for in SEM: intra-element, continuous variations approximated by their projection on the high degree (typically $N \in [4-6]$) local polynomial bases, and inter-element discontinuities, thank to the FEM functional framework. Note that the representation of small-scale variations by the local spectral element polynomial bases is intrinsically limited. Trying to represent localized variations, for example material discontinuities, can lead to aliasing effects and/or Gibbs oscillations just like in the traditional spectral methods (e.g. Boyd 2001). However, practical situations occur where discontinuities exist but can hardly be represented at the discrete level due to geometrical complexity in the design of hexahedral meshes (e.g. when large variations of interface elevation occur on small spatial scales) or due to prohibitive computational cost to respect the Courant–Friedrichs–Lewy (CFL) stability condition (e.g. close to the valley or basin edges). Some approximate mesh design strategies are sometimes adopted in those cases. In these strategies, the element boundaries do not follow the shape of the material interfaces (they do not coincide with the interfaces). We may use acronym ‘NF’ (not following) for these strategies. In the remainder of the paper, the performance of some NF strategies is evaluated and compared to

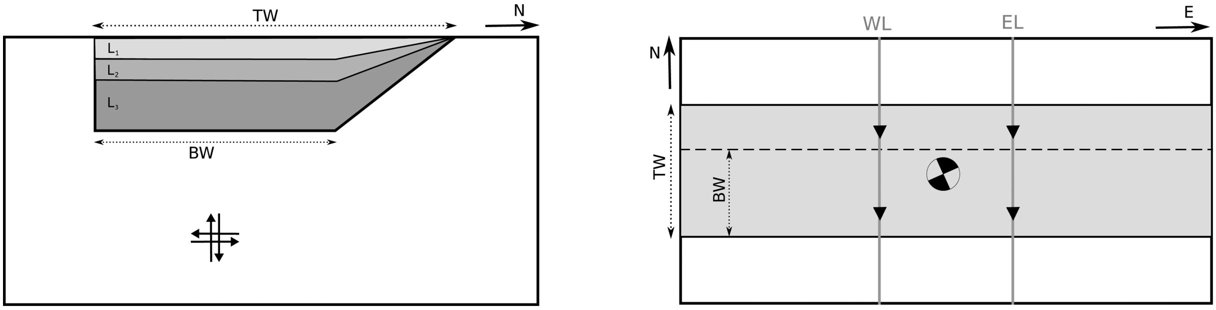

Figure 11. Schematic representation (left: vertical cross-section, right: surface view) of the valley model used in the test cases 2D-sharp and 2D-smooth. The bottom and total widths are BW = 3.5 km and TW = 5 km, respectively, and the maximum sediment thickness is about 205 m. The location of the source is indicated by the double-couple in the left figure and by the beach ball in the right one. The triangles along the western line (WL) and eastern line (EL) indicate the receiver positions where numerical predictions are further compared.

the optimal strategy, referred to as ‘F’ strategy, in which the element boundaries follow the interfaces (i.e. material interfaces never intersect the elements). Note that the spectral element meshes considered here are always geometrically conforming, that is such that neighbouring elements share either a corner or an entire edge or face.

Two open-source codes implementing SEM have been used in this study: `specfem3D` (Peter *et al.* 2011) and `efispec` (De Martin 2011). Both codes implement the P1 paraxial formulation of Stacey (1988) at the absorbing boundaries. We always used a polynomial order $N = 5$ and, away from the interfaces, we imposed the size of the spectral elements to be smaller than or equal to the local minimum S wavelength. The results obtained with the two codes are strictly similar when using the same mesh of elements. In the remainder of the paper, the results obtained with `specfem3D` (resp. `efispec`) will be referred to as SEM1 (resp. SEM2).

4.2 FPSM

The FPSM combines the optimal accuracy of the global spectral differential operators with the simplicity of the spatial discretization using a structured rectangular grid. The peculiarity of FPSM consists in the evaluation of the spatial derivatives by means of a multiplication in the wavenumber domain. Time evolution is usually solved using non spectral approaches, as, for example the 2nd-order explicit finite-difference scheme used in this paper. The transition from the spatial domain to the wavenumber domain, and back, is performed by means of the fast Fourier transform. Thanks to the Nyquist sampling theorem, FPSM works with a relatively coarse spatial sampling (Fornberg 1987), which represents a valuable advantage when solving 3-D problems.

On the other hand, the nature of the global differential operators implies that possible numerical artifacts are spread across the whole space domain. There are two common sources of numerical errors. One is the discontinuity of the fields that are being differentiated, which produces singularity in the calculated wavefield (Gibbs phenomenon). The other is the representation of material discontinuities (interfaces): since FPSM solves the heterogeneous formulation of the equation of motion, artefacts may be due to the staircase approximation interfaces with sharp impedance contrast. The free-surface condition—a typical feature of models used for earthquake ground motion simulations—can be seen as an extreme case of a sharp material interface and therefore is particularly challenging for FPSM.

The FPSM implementation used in this paper (Klin *et al.* 2010) tackles the aforementioned problems in the following way. The occurrence of Gibbs phenomenon is significantly reduced using the Fourier differential operators on staggered grids (Őzdenvar & McMechan 1996). The staircase approximation of the material interfaces is avoided using the volume harmonic averaging of the elastic moduli and volume arithmetic averaging of density proposed by Moczo *et al.* (2002). The free-surface boundary condition—discontinuity of displacement and vanishing traction at the free surface—is solved by the following approach: (1) before applying the differential operator a linear function is subtracted from the displacement field in order to remove its discontinuity at the free surface, and it is added back after differentiation is performed; (2) a stress imaging technique accomplishes the vanishing of the stress field. In order to sample adequately the surface wave wavefield, which features higher vertical-component wavenumbers close to the free surface, the vertical spatial sampling step is gradually squeezed towards surface. Finally, the wavefield absorption at lateral and bottom boundaries of the computational domain is performed with the convolutional perfectly matching layer (CPML; Komatitsch & Martin 2007).

A more comprehensive review of FPSM and related discussions can be found in Klin *et al.* (2010) and Moczo *et al.* (2014).

4.3 3-D (2-4) Velocity–stress finite-difference scheme on an arbitrary discontinuous staggered grid (FDM-S)

Here we very briefly describe the finite-difference methodology that has been developed based on several partial approaches starting from the introduction of the staggered-grid schemes into seismology (Madariaga 1976; Virieux 1984, 1986) up to developing the orthorhombic effective grid modules (Moczo *et al.* 2014). Because the description of the methodology below is very concise, we refer for a complete theory to the book by Moczo *et al.* (2014).

The scheme solves the strong differential form of the equation of motion and time derivative of Hooke’s law for the viscoelastic medium with rheology of the generalized Maxwell body. The schemes have the same structure as standard velocity–stress staggered-grid schemes which are 2nd-order accurate in time and 4th-order accurate in space. The accuracy of the scheme in the heterogeneous medium is mainly determined by the way how a smooth material heterogeneity and material interface are represented by the effective material grid parameters. Two approaches are applied in this study. The first one has been presented by Moczo *et al.* (2002). The effective grid density is evaluated as an integral volume arithmetic average of density inside a grid cell centred at the grid position of the corresponding particle velocity component. The effective grid unrelaxed bulk and shear moduli are evaluated as integral volume harmonic averages of moduli in respective grid cells centred at grid positions of the stress-tensor components. The integrals are evaluated numerically and the grid cell can contain a material interface. In the second approach, the effective averaged medium has, in general, an orthorhombic anisotropy. If a material interface is parallel to a Cartesian coordinate plane, the averaged medium is transversely isotropic. The transverse anisotropy is the correct representation of a planar material interface consistent with the boundary conditions in the long wavelength approximation (as shown originally by Backus (1962) and discussed also by Moczo *et al.* (2002)). For a detailed exposition see chapter 9 of the book by Moczo *et al.* (2014). The free surface is simulated using the AFDA technique (Kristek *et al.* 2002; Moczo *et al.* 2004). The non-reflecting boundaries of the spatial grid are simulated by using PML. For efficient modelling of earthquake motion in surface sedimentary structures a spatially discontinuous staggered grid is used. The stable algorithm of the discontinuous grid (Kristek *et al.* 2010) enables one to use the ratio between the bottom coarser grid and upper finer grid as large as 25. For the computer codes we refer to `http://www.nuquake.eu/FDSim` (last accessed 16 January 2015).

4.4 3-D Velocity–stress collocated-grid finite-difference method (FDM-C)

The FDM-C (Zhang & Chen 2006; Zhang *et al.* 2012) solves the first-order hyperbolic velocity–stress elastodynamic equations using finite-difference approximations with all the wavefield components and model parameters defined at the same grid point. Having quantities collocated, the method is well suited to utilize curvilinear grids for solving elastodynamic equations in curvilinear coordinates. This makes it suitable for implementing irregular free surface. The collocated grid is also a natural choice to simulate seismic waves in a general anisotropic medium. A simple application of the central differences on the collocated grid to approximate the first-order derivative would lead to odd-even decoupling problem as a grid-to-grid oscillation in the simulation results. Either a spatial filtering or artificial damping would be necessary to suppress the non-physical grid-to-grid oscillations. The FDM-C in this paper uses the DRP/opt MacCormack scheme (Hixon 1998) with a 7-point stencil for one derivative. Usually the accuracy of a 7-point stencil can reach 6th order. However, in the DRP MacCormack scheme, two points are sacrificed to achieve optimal dispersion accuracy by the dispersion-relation preserving (DRP) methodology (Tam & Webb 1993), which results in an optimized 4th-order accuracy in terms of dispersion error. To get minimal dissipation error, DRP/opt MacCormack of (Hixon 1998) optimizes the coefficients of the DRP MacCormack at 8 points per wavelength and higher. In the DRP/opt MacCormack scheme, the central spatial difference operator is split into forward and backward one-sided difference operators, which are alternately used in the 4th-order Runge-Kutta time marching schemes. The one-sided operators introduce inherent dissipation, which can damp the spurious short-wavelength numerical (non-physical) waves to avoid the odd-even decoupling. The central difference is recovered when the forward and backward differences are added together. As we can use different operators in three dimensions, there are in total eight biased different operators, and they are used sequentially in an 8-steps cycle to get minimal error. More details can be found in Zhang & Chen (2006) and Zhang *et al.* (2012). The free-surface boundary condition on curvilinear grids is implemented by the traction-imaging method (Zhang & Chen 2006; Zhang *et al.* 2012) which antisymmetrically images the traction components to the ghost points and is an extension of the stress-imaging technique for the flat free surface. For a discrete representation of material heterogeneity, the effective media approach by Moczo *et al.* (2002) is adopted. The density at a point is evaluated as the volume arithmetic average whereas λ and μ at a point are calculated as the volume harmonic averages. PML is used as the absorbing technique surrounding the lateral and bottom boundaries. If the grid is rectangular in the absorbing layers, the auxiliary differential equations implementation of the complex frequency-shifted PML (ADE CFS-PML; Zhang & Shen 2010) is used. If the grid is curvilinear in the absorbing zones, a multi-axial extension (ADE CFS-MPML) towards stable simulations on curvilinear grids (Zhang *et al.* 2014) is applied.

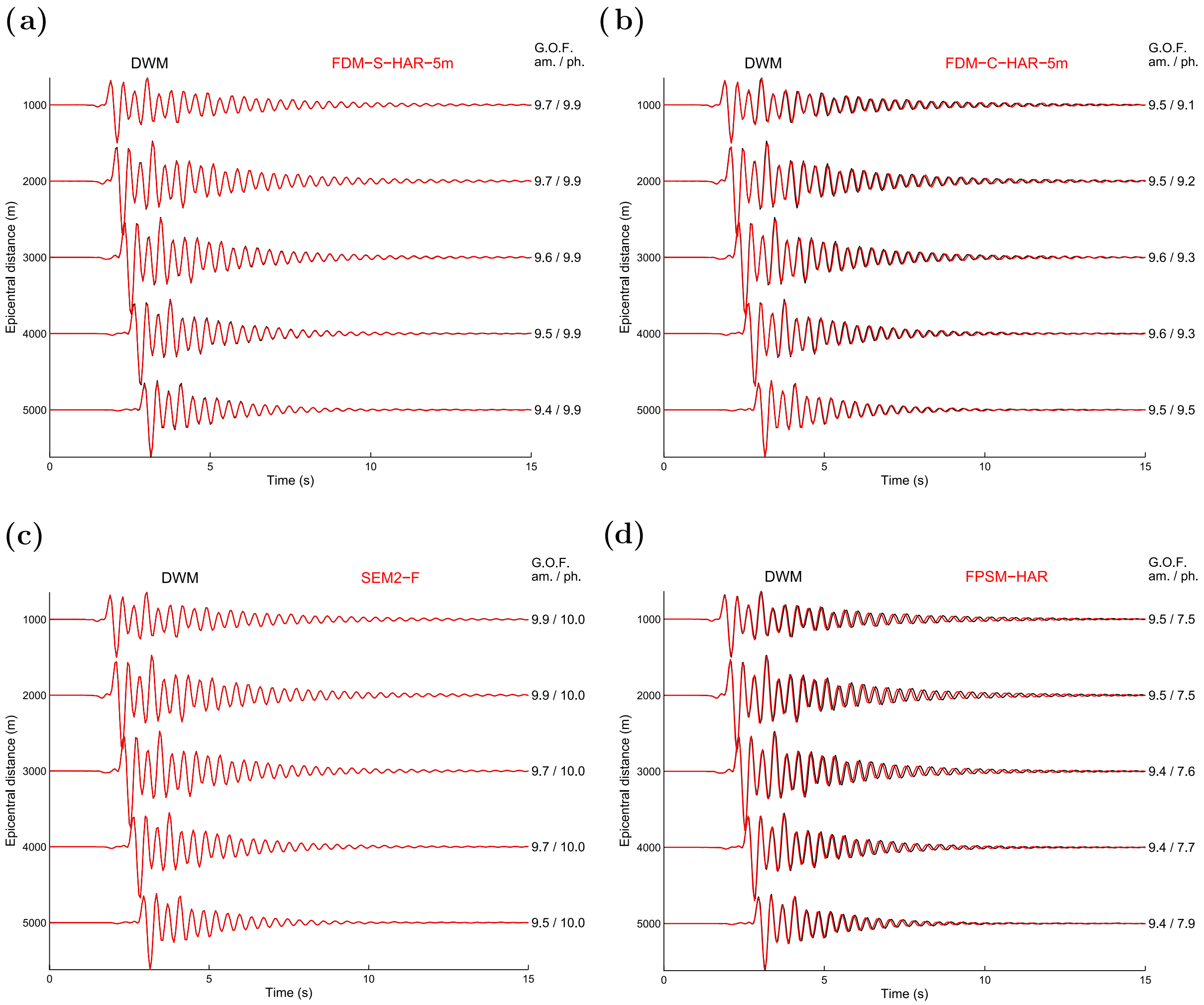

Figure 12. East–west component of ground velocity along the northern surface profile computed for the 1D-sharp case by 4 different methods: (a) FDM-S; (b) FDM-C; (c) SEM2-F; (d) FPSM. HAR indicates the harmonic averaging of the elastic moduli. Each of the seismograms (plotted in red) is superimposed on the reference solution computed with DWM (in black). The numbers to the right of each trace correspond to the goodness-of-fit scores in envelope (labelled to as 'am') and phase (labelled to as 'ph') with respect to the reference solution. A perfect match corresponds to a score of 10.

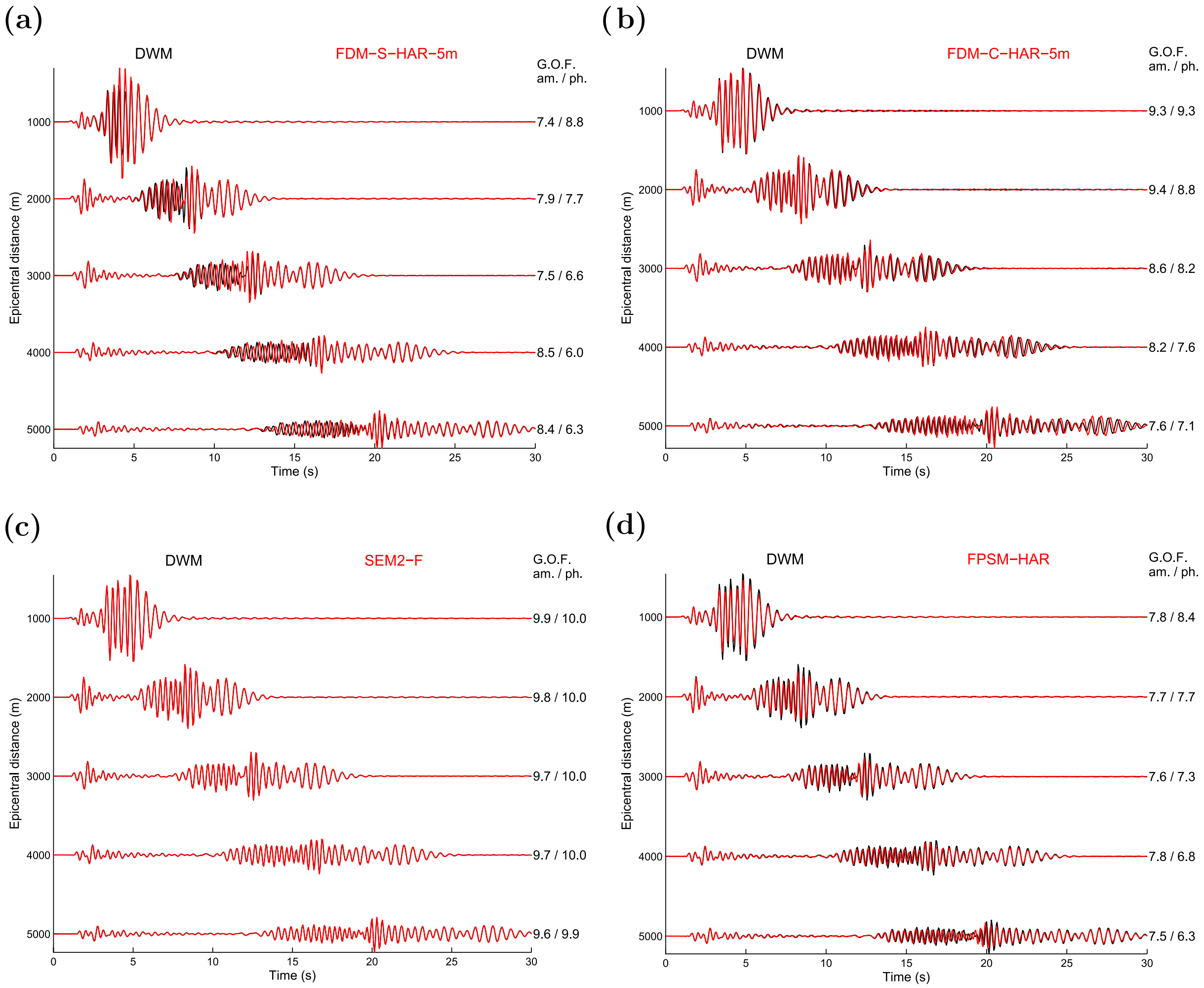

Figure 13. Same as Fig. 12 for the vertical component of ground velocity.

5 RESULTS FOR 1-D GEOMETRY

5.1 1-D layered model with sharp interfaces

Fig. 12 shows the EW component of ground velocity along the northern surface profile (Fig. 5) computed for the 1D-sharp case by the four methods: FDM-S, FDM-C, FPSM and SEM2-F. Note that in FDM-S, FDM-C and FPSM calculations, the volume harmonic averaging of the elastic moduli and volume arithmetic averaging of mass density proposed by Moczo *et al.* (2002) is used to approximate the physical interfaces of the 1D-sharp model, and that the SEM2-F calculations are performed following the F strategy, that is imposing that the interfaces of the model coincide with the spectral elements' boundaries. In FDM-S and FDM-C, the grid spacing is 5 m, which corresponds to a minimum of 10 gridpoints per S wavelength at the surface. The horizontal grid spacing is 20 m for FPSM and 10 m in average for SEM2-F at the surface (i.e. the horizontal size of the surface spectral elements is 50 m and the polynomial order is $N = 5$). The vertical grid spacing increases in FPSM from 3 m at the surface to 100 m in the bedrock. In SEM2-F it is set in average to 3.46 m in the first layer and to 14.5 m in the second layer. The spectral element mesh is further coarsened twice with depth using a three-to-one elementary brick (e.g. Peter *et al.* 2011), yielding an average horizontal and vertical resolution of 90 m in the bedrock. Each numerical solution is superimposed on the reference one–computed with DWM as detailed in Section 3.1.1. The goodness-of-fit (GOF) in amplitude and phase between the two solutions are also shown. The GOF values were obtained as

$$G = 10\exp(-|M|),$$

where M represents the time-frequency misfit in amplitude or phase evaluated for the time-frequency window $[0 - 30]\,\mathrm{s} \times [0 - 4]\,\mathrm{Hz}$. G attains values from 0 (no fit) to 10 (perfect fit); see Kristeková *et al.* (2009) for details. As expected from the spatial resolution used and given the fact that the analysed traces contain only body waves, the level of agreement obtained in Fig. 12 is excellent with amplitude GOF values well above 9 for all solutions, and with only FPSM exhibiting non-optimal phase GOF values, slightly below 8.

The same comparison for the vertical component of ground velocity is shown in Fig. 13. Except for the SEM2-F calculations, clear differences in phase and amplitude are now seen in all the predicted surface wave trains. Whereas for the solutions computed with FDM-S and FPSM the phase error seems to increase with frequency, it looks more uniformly distributed for the FDM-C solution. The overall GOF scores are, however, similar for the three solutions. They are even slightly higher for the FDM-C solution which, surprisingly, shows a minimal phase error on the high-frequency Airy phase of the fundamental Rayleigh mode. Note that the GOF values decrease with epicentral distance as expected from the accumulation of error during propagation.

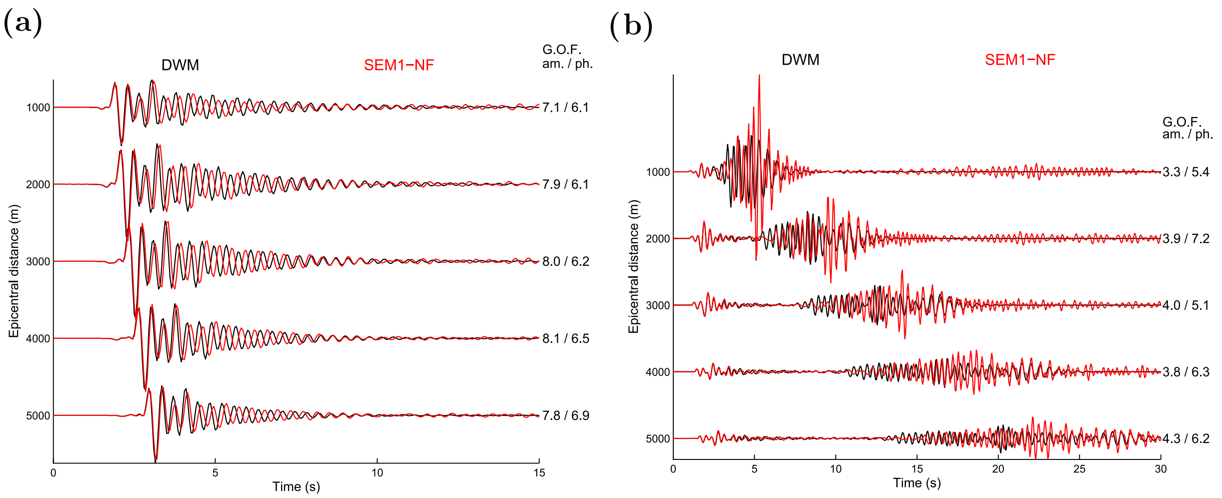

Figure 14. East–west (left-hand panel) and vertical (right-hand panel) components of ground velocity computed for the 1D-sharp case using SEM1-NF.

The excellent fit obtained for SEM2-F is intrinsically related to the correct discrete representation of the interfaces in the 1D-sharp model by the F strategy. In Fig. 14, we present the results obtained with SEM1 using a NF strategy, where instead of squeezing one element in the first layer, L_1, two spectral elements of the same vertical size (= 44.9 m) are used to describe the first two layers, L_1 and L_2. Note that only the first physical interface is approximated in this modified mesh, the other two still coincide with elements'

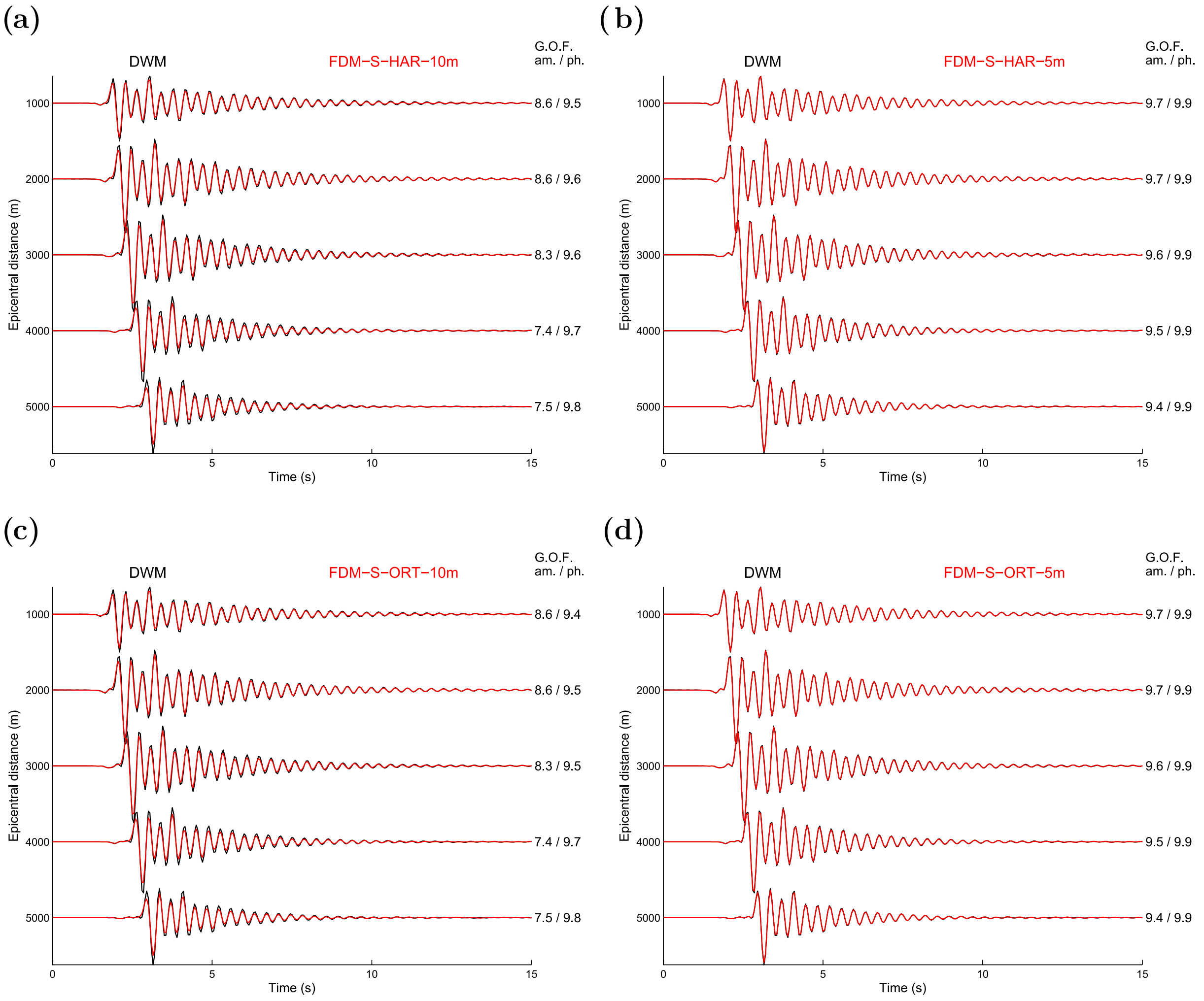

Figure 15. East–west component of ground velocity along the northern surface profile for the 1D-sharp case computed with FDM-S using different grid spacings and definitions of the effective media: (a) harmonic averaging, 10 m; (b) harmonic averaging, 5 m; (c) orthorhombic averaging, 10 m; (d) orthorhombic averaging, 5 m.

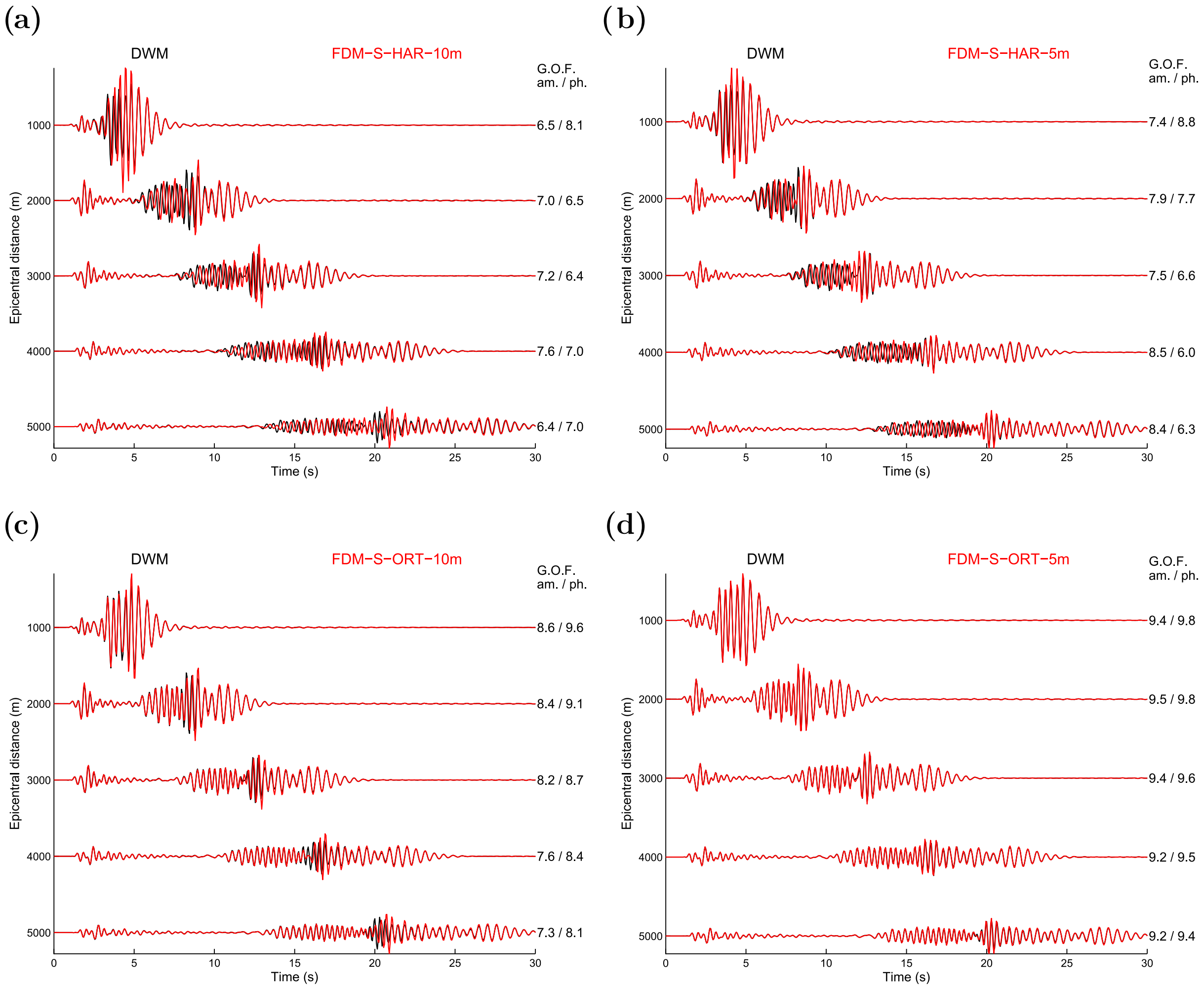

Figure 16. Same as Fig. 15 for the vertical component of ground velocity.

boundaries (i.e. the vertical size of the elements is further adapted to the thickness of the L_3 layer). The effect on the accuracy of the resulting numerical solution is tremendous. Apart from the direct *S* wave, all the other arrivals are affected by large phase and amplitude errors: the high-frequency 1-D resonance occurs at a slightly lower frequency (around 2.5 Hz instead of 2.7 Hz) and the surface wave dispersion pattern is completely different. This is not a straightforward matter of the vertical spatial resolution in terms of the number of nodes per wavelength, but rather a problem of how the discontinuity in the material parameters is represented at the discrete level by the local spectral polynomial bases: everything happens as if we had computed an accurate solution in a wrong discrete model. Note that some of the inaccurate late arrivals in the SEM1-NF solution (e.g. around 20 s at 1 km epicentral distance) are due to weak reflections off the western (not perfectly absorbing) boundary of the computational domain, which was not as distant as in the mesh used in computation of the reference SEM2-F solution. Those spurious arrivals, however, contribute only marginally to the misfit with the reference solution.

The sensitivity of the surface wave dispersion properties on the discrete implementation of the model in SEM was reported by Capdeville & Marigo (2008) in the context of global seismology. It can be recast under the general issue, faced by any grid-based numerical method, of how to represent spatial variations of the elastic parameters which are smaller than the size of the numerical grid cell (the extreme case being that of a material discontinuity). The main challenge is to 'up-scale' the medium, that is to design an effective medium which realizes a physically consistent, low-pass filtering of the original model. Several up-scaling procedures have been derived in the last years: Moczo *et al.* (2002) proposed to use the volume harmonic average of the elastic moduli and arithmetic average of the mass density in the vicinity of a material discontinuity; Fichtner & Igel (2008) presented a non-linear minimization approach to design smooth models which preserve the phase velocities of a few target Love and Rayleigh modes; more recently Capdeville *et al.* (2010a,b) and Guillot *et al.* (2010) introduced a general numerical procedure to derive a fully anisotropic effective model using the framework of the homogenization theory; Moczo *et al.* (2014) extended their 2002 formulation to a more general effective medium with the orthorhombic anisotropy.

In Figs 15 and 16, we illustrate the performance of this new orthorhombic effective medium for numerical solutions for the 1D-sharp case computed with FDM-S. Note that because the interfaces are horizontal, the anisotropy simplifies to the vertical transverse isotropy, that is, the effective medium reduces to the one predicted by Backus (1962). For the seismograms consisting of body waves crossing the discontinuities (Fig. 15), the two approaches are comparable, the accuracy being controlled by the resolution of the grid rather than by the choice of the effective medium. The advantage of using the orthorhombic approach is much clearly seen in Fig. 16, which involves Rayleigh waves propagating parallel to the

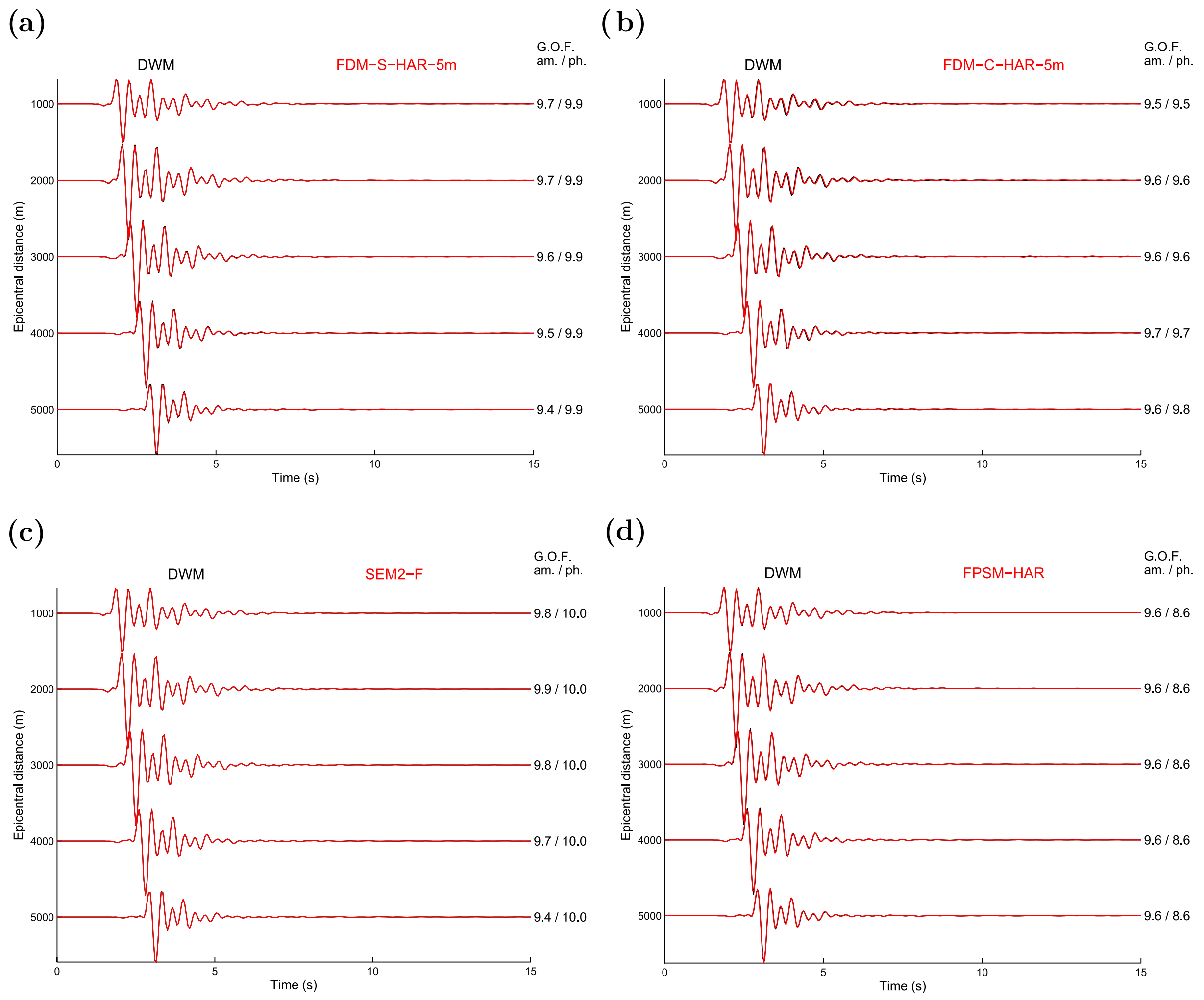

Figure 17. East–west component of ground velocity along the northern surface profile computed for the 1D-smooth case by four different methods: (a) FDM-S; (b) FDM-C; (c) SEM2-F; (d) FPSM.

discontinuities: the anisotropic solution computed with a grid spacing of 10 m (Fig. 16c) outperforms the isotropic solution obtained with a grid spacing twice smaller (Fig. 16b), having inaccuracy only in the high-frequency Airy phase of the fundamental Rayleigh mode. Further reducing the grid spacing to 5 m in the anisotropic solution (Fig. 16d) allows to reach the same level of accuracy as with SEM2-F.

Note that the applied number of grid points per wavelength in the 1D-sharp model may not be sufficient in other (velocity) models for obtaining the same level of accuracy.

5.2 1-D gradient layer model

The numerical solutions for the 1D-smooth case computed with the four methods (FDM-S, FDM-C, FPSM and SEM2-F) are shown in Fig. 17 (EW component) and Fig. 18 (vertical component). Compared to the 1D-sharp case, the level of goodness-of-fit with respect to the reference solution is systematically increased for both body and surface waves.

Most interestingly, the solution obtained with SEM1-NF, in which the mesh design follows the NF strategy, is also sufficiently accurate, as shown in Fig. 19. This is related to the ability of the polynomial bases used in the shallow spectral elements to represent the 1D-smooth velocity model, which consists of a gentle kink—the *S* velocity gradients in layers L_1 and L_2 are 2.89 and 3.45 s^{-1}, respectively. The comparison of the FDM-S solutions obtained with different effective medium implementations and grid spacings is shown in Fig. 20. The same conclusion drawn for the body waves in the 1D-sharp model, that numerical accuracy was mostly controlled by the resolution of the grid rather than by the choice of the effective medium, now applies to the entire simulated wavefield.

The comparison suggests that the material interface of the first order (discontinuity of the first derivative only) does not produce significant effective anisotropy.

6 RESULTS FOR 2-D GEOMETRY

We now consider more realistic canonical cases with a 2-D geometry. The aim of this section is to highlight how the discrete representation of the model, in particular at valley edges, where surface waves are generated, influences the accuracy of the numerical prediction of earthquake ground motion.

6.1 2-D valley with sharp interfaces

We first consider the 2D-sharp model with geometry shown in Fig. 11. The flat part corresponds to the three-layer-over-half-space model 1D-sharp.

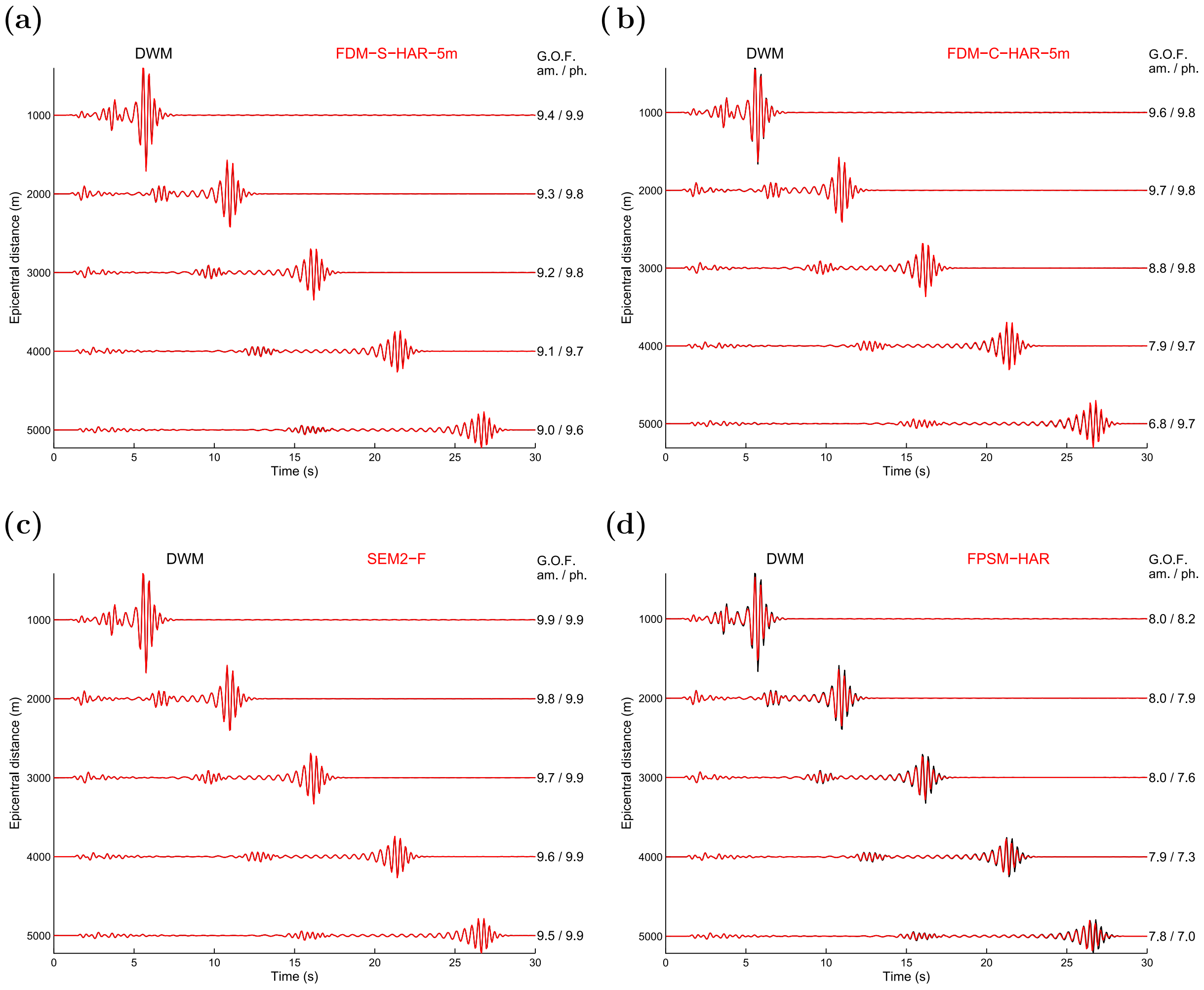

Figure 18. Same as Fig. 17 for the vertical component of ground velocity.

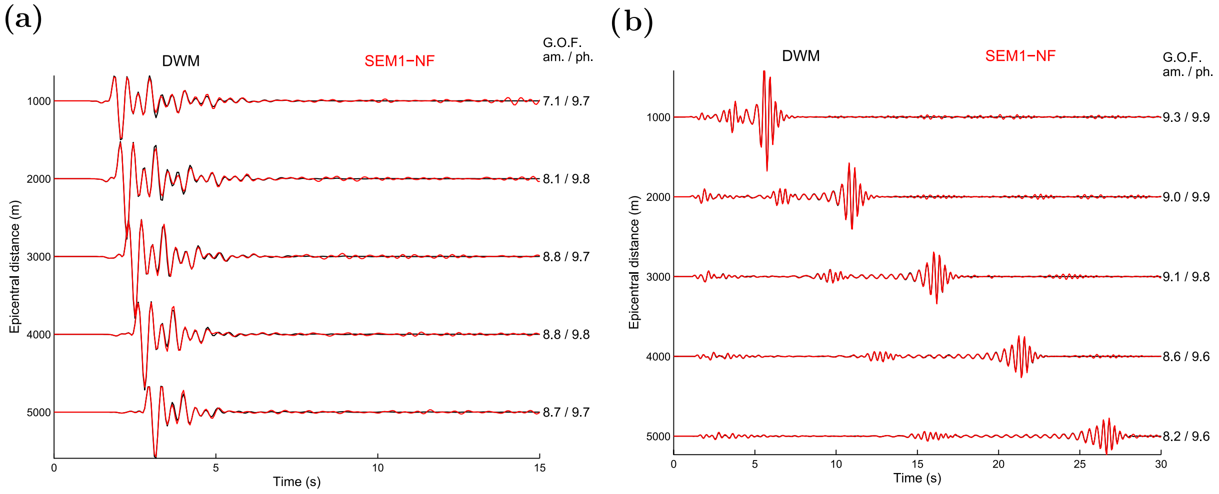

Figure 19. East–west (left-hand panel) and vertical (right-hand panel) components of ground velocity for the 1D-smooth case computed with SEM1-NF.

Relying on the results for the 1D-sharp case, we consider as a reference the solution computed with SEM2-F with the mesh (shown in Fig. 21) designed following the F strategy. Because of the deformation of the hexahedra close to the northern edge of the valley, the distance between the grid points tends towards a very tiny value, yielding an extremely severe CFL stability condition on the time step. In such realistic situations, the F strategy can drastically decrease the computational efficiency of SEM. In the remainder of the paper, some alternative strategies are presented and their efficiency is discussed.

The seismograms of the SEM2-F solution are shown in Fig. 22 for two horizontal components along two different surface profiles.

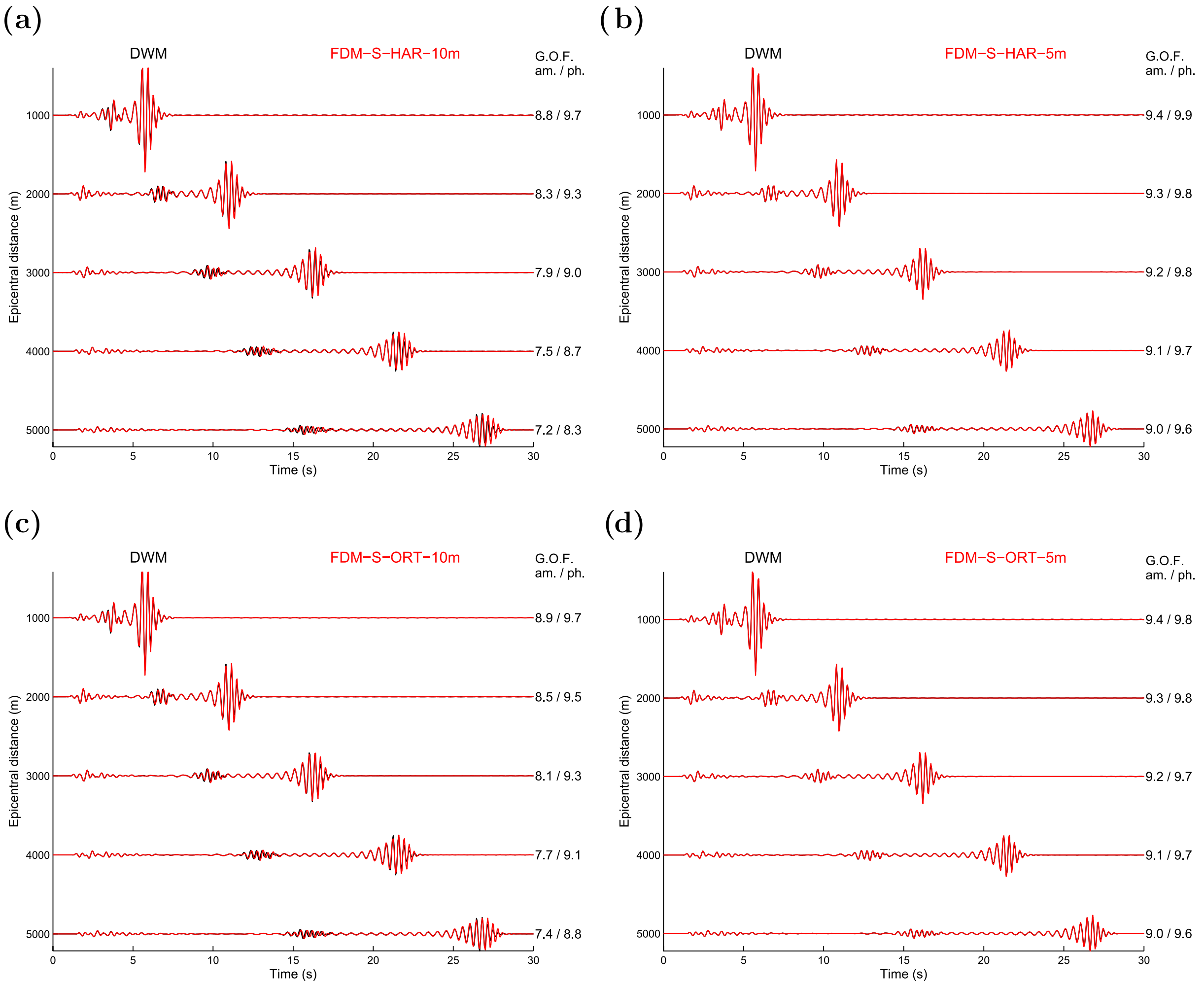

Figure 20. Vertical component of ground velocity along the northern surface profile for the 1D-smooth case computed with FDM-S using different grid spacings and definitions of the effective media: (a) harmonic averaging, 10 m; (b) harmonic averaging, 5 m; (c) orthorhombic averaging, 10 m; (d) orthorhombic averaging, 5 m.

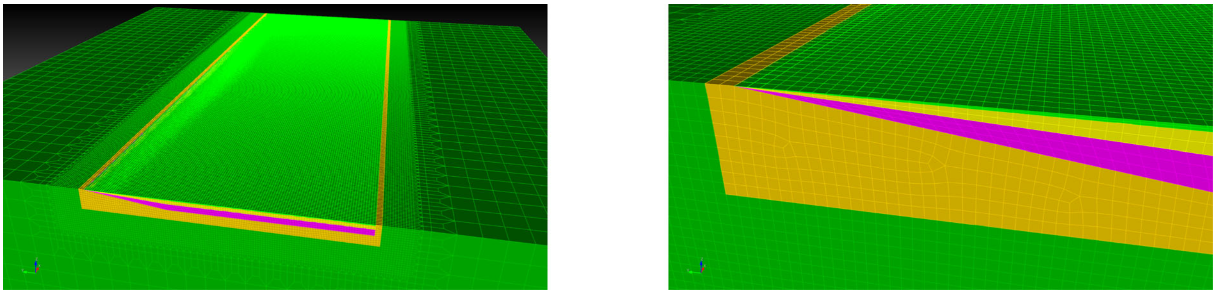

Figure 21. Spectral element mesh, designed following the F-strategy, used to compute a reference solution of the 2D-sharp case. The mesh consists of a 2-D section of unstructured quadrilaterals which is further ‘swept’ along the direction transverse to the valley in order to define hexahedra. The mesh is further coarsened in the horizontal and vertical directions, from the orange ‘shoe-box’ intermediate region to the outside green region.

Because the model has a 2-D geometry, the left seismic section is dominated by the in-plane component of motion corresponding to a pseudo-2-D *P–SV* case (the wavefield would be fully 2-D if it was excited by a line of sources parallel to the axis of the valley) and the right section by the out-of-plane component of motion corresponding to a pseudo-2-D *SH* case. A clear asymmetry in the excitation of surface waves is observed between the edges of the valley. At the (northern) edge with the gentle slope, very energetic and strongly dispersed Rayleigh and Love surface waves are generated, whereas the surface wave trains generated at the vertical (southern) edge are hardly seen. The red lines indicate the seismic traces that are used as reference for comparing with the other numerical predictions. They correspond to receivers located 1 km away from the edges of the valley.

Fig. 23 shows the horizontal in-plane component of the ground motion computed at the northern receiver by FDM-S, FDM-C, FPSM and SEM1-BE. The numerical solutions were computed using the same spatial resolution as for the 1D-sharp case, except for

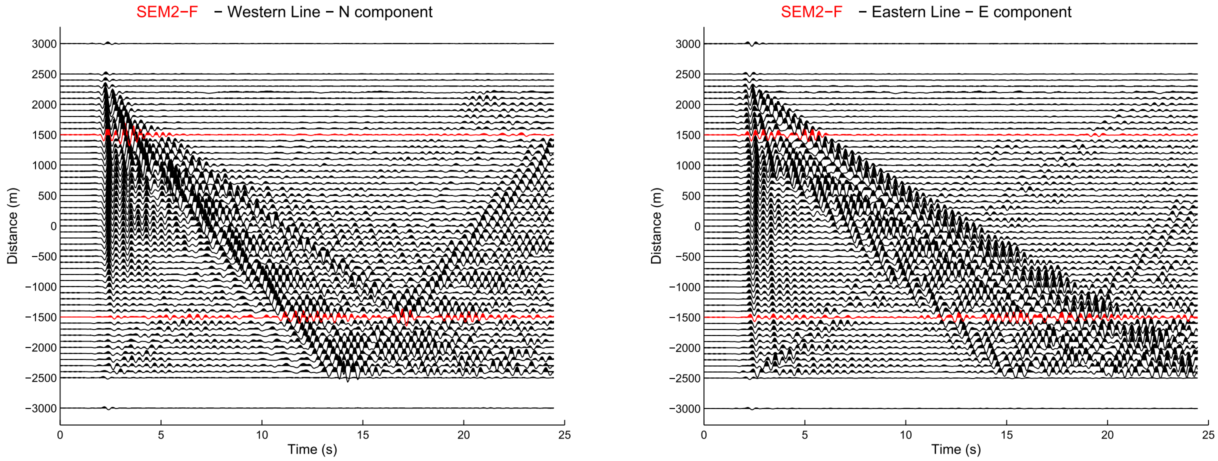

Figure 22. Seismic sections of the north–south (left-hand panel) and east–west (right-hand panel) components of ground velocity along the western (left-hand panel) and eastern (right-hand panel) profiles (Fig. 11) computed for the 2D-sharp case with SEM2-F. The distance is measured from the centre of the valley and increases towards north. The left (resp. right) panel shows a strongly dispersed Rayleigh (resp. Love) wave train excited at the northern edge. Red traces correspond to locations where the different numerical predictions are further compared (see text).

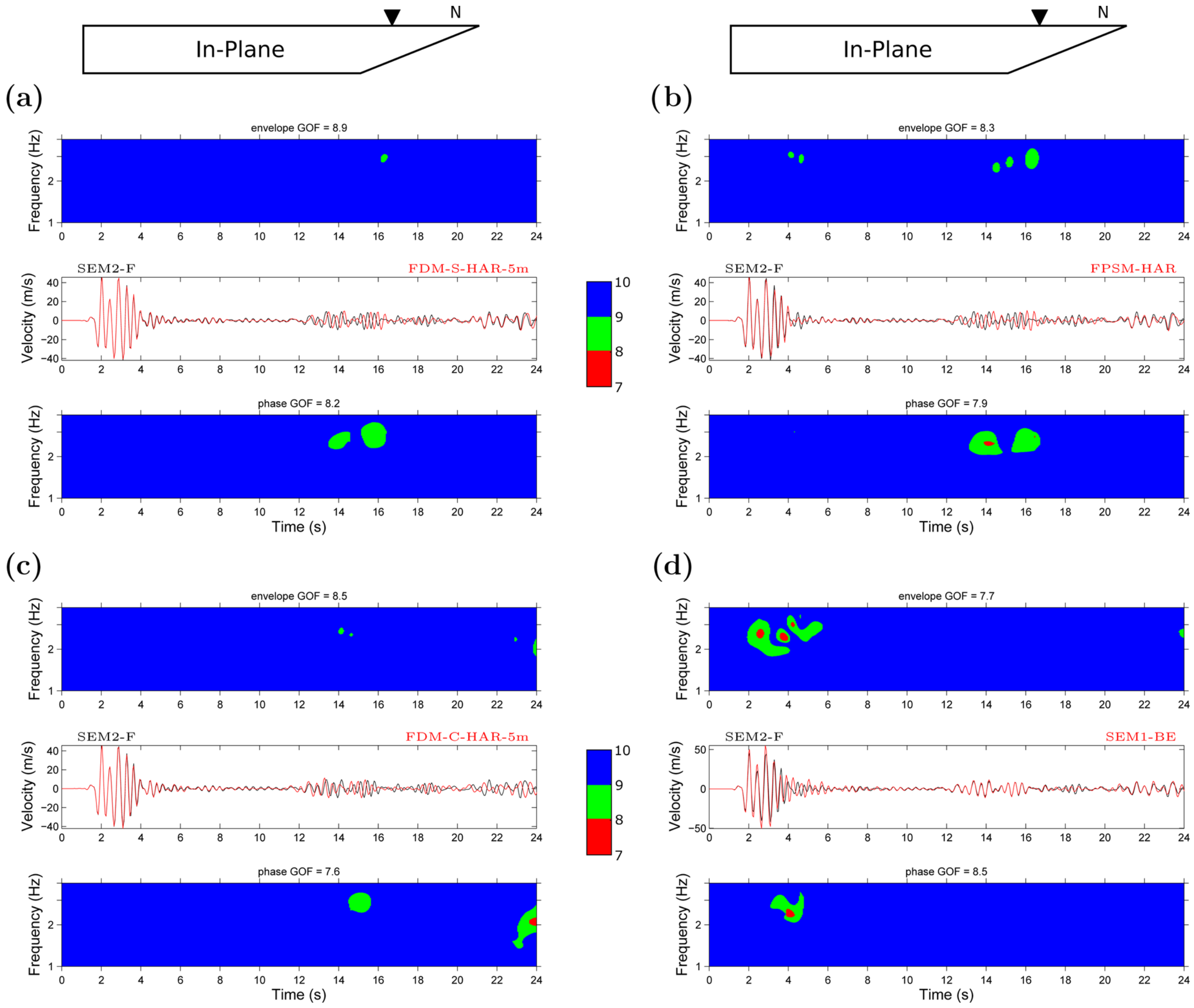

Figure 23. North–south component of ground velocity at a receiver along the western surface profile of Fig. 11, 1 km away from the northern edge, computed for the 2D-sharp case by four teams using (a) FDM-S, (b) FPSM, (c) FDM-Cand (d) SEM1-BE. The SEM2-F solution is taken as a reference and is plotted in black. The level of agreement between each solution and the reference is quantified by the time-frequency goodness-of-fit (GOF) in amplitude (top panel) and phase (bottom panel). The colour scale indicates the level of GOF, from 7 to 10 (perfect fit). The average GOF is indicated on top of the time-frequency subplots.

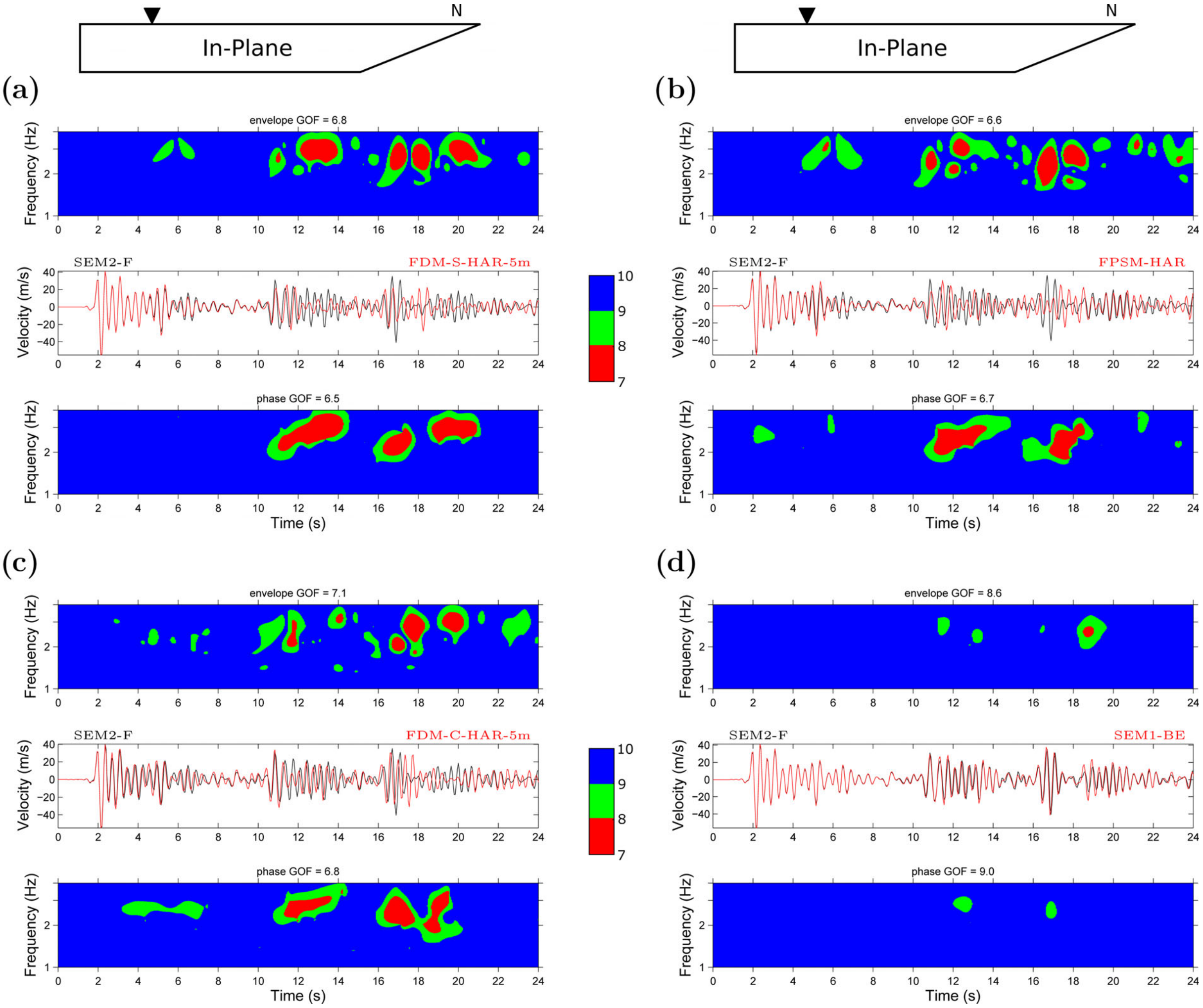

Figure 24. Same as Fig. 23 at a receiver which is 1 km away from the southern edge of the valley.

FPSM where the vertical grid spacing varies from 7 m (instead of 3 m) at the surface to 84 m (instead of 100 m) in the bedrock. In the SEM1-BE solution, the mesh is designed in the ‘best-effort’ (BE) mode, which is a compromise between the F and NF strategies: the boundaries of the elements follow the material interfaces only when these are horizontal or vertical. This results in a ‘shoebox’ high-resolution mesh coinciding at the southern edge with the mesh designed following the F strategy, but with elements intersected by the material interfaces at the northern edge. Note that the BE strategy makes it possible to increase the time step compared to the F strategy, and consequently decrease the total CPU time of the calculation, by a factor $p \simeq 13$.

Each prediction in Fig. 23 is superimposed on the SEM2-F reference, and the time-frequency GOF (in amplitude and in phase) with respect to the reference are shown as colour images. The agreement with the reference is very good, even excellent in the first arrival, around 2 s. Some discrepancies appear around 3 s, in the Rayleigh waves generated at the nearby northern edge, for the FPSM solution and more noticeably for the SEM1-BE solution which, among all solutions, is the one that makes the crudest approximation of the northern edge geometry. The level of GOF generally decreases with time, except for the SEM1-BE solution because the BE strategy used to design the mesh is optimal to accurately model the generation of Rayleigh waves at the southern edge and their propagation along the flat part of the valley.

In Fig. 24, we compare the same horizontal in-plane component of ground motion but at the southern receiver. The agreement is very good for the first 10 s of the seismogram which consists of body and Rayleigh waves generated at the vertical southern edge. The level of agreement considerably decreases for later arrivals consisting of Rayleigh waves excited at the northern edge of the valley. The best fit is obtained with the SEM1-BE solution, suggesting that the error in the numerical modelling of the surface wave generation at the northern edge is not increased by the propagation of the surface waves towards the centre of the valley. For all the other solutions, the numerical error accumulates during propagation of the surface waves along the horizontal interfaces—as in the 1D-sharp case. Note that the phase of the FDM-C solution seems again optimally accurate for the most energetic Rayleigh surface wave arrivals around 11 and 17 s, which probably correspond to Airy phases.

In Fig. 25 we compare the horizontal in-plane component at the southern receiver computed with FDM-S for different resolutions and definitions of the effective medium. As in the 1D-sharp case, the advantage of using the orthorhombic effective medium is clearly seen on the late Rayleigh waves generated at the northern edge: the GOF levels for the anisotropic solution computed with 10 m grid spacing (Fig. 25c) are much higher than for the 5 m isotropic solution (Fig. 25b). Halving the size of the grid in the anisotropic solution (Fig. 25d) yields perfect match with the SEM2-F solution,

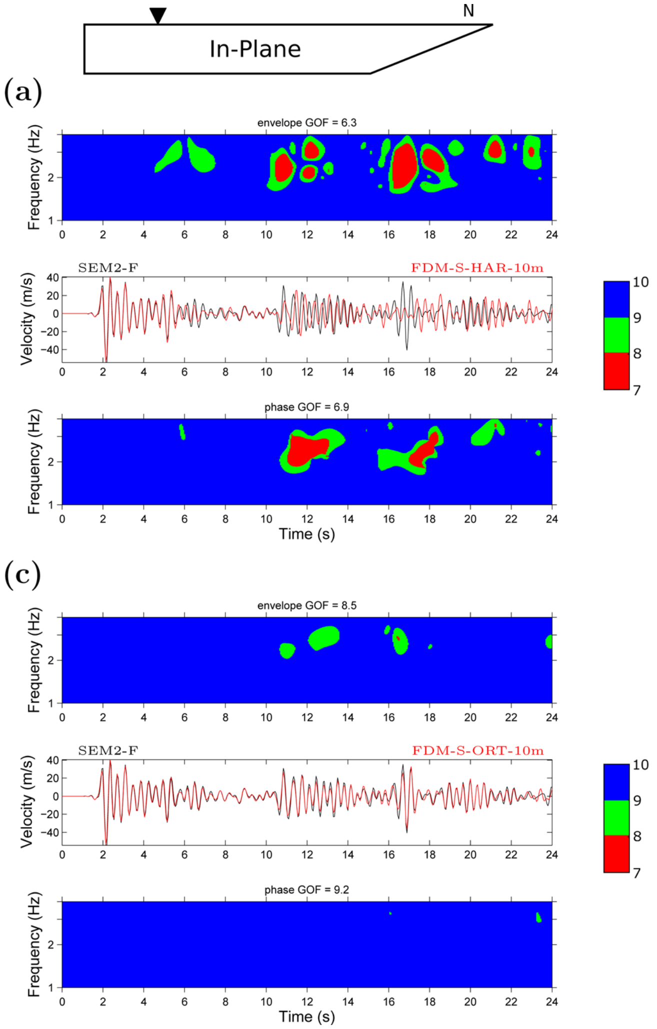

Figure 25. Same as Fig. 24 for solutions computed with FDM-S using different grid spacings and definitions of the effective medium: (a) harmonic averaging, 10 m; (b) harmonic averaging, 5 m; (c) orthorhombic averaging, 10 m; (d) orthorhombic averaging, 5 m.

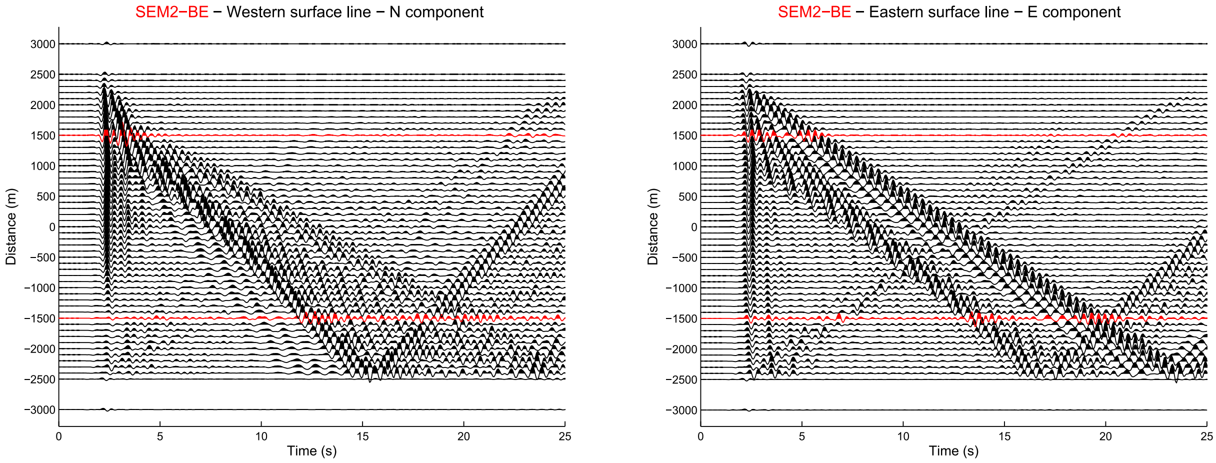

Figure 26. Seismic sections of the north–south (left-hand panel) and east–west (right-hand panel) components of ground velocity along the western (left-hand panel) and eastern (right-hand panel) profiles (Fig. 11) computed with SEM2-BE for the 2D-smooth case. The distance is measured from the centre of the valley and increases towards north. The left (resp. right) panel shows strong Rayleigh (resp. Love) wave trains excited at the northern edge. Red traces correspond to locations where the different numerical predictions are further compared.

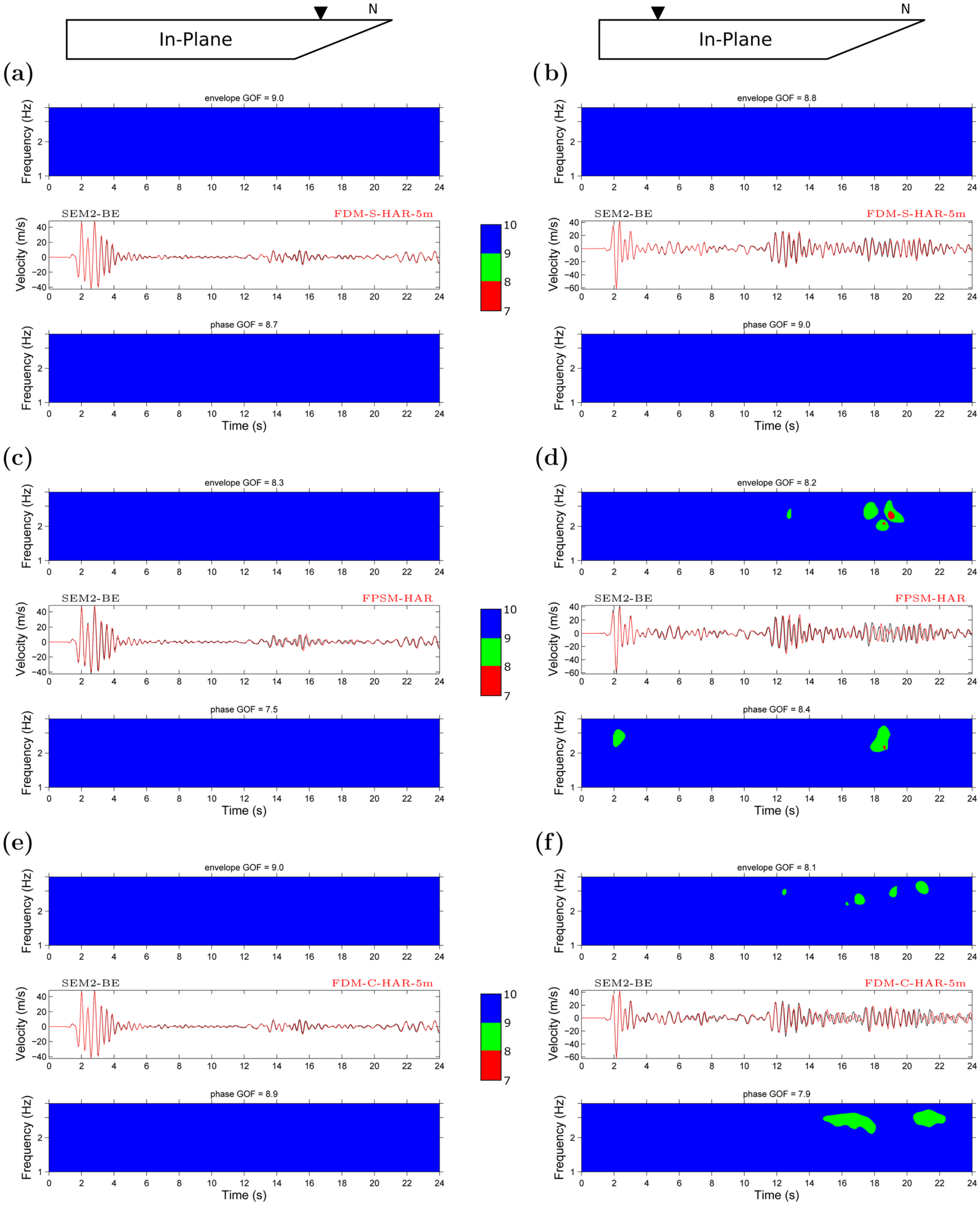

Figure 27. North–south component of ground velocity at receivers along the western surface profile of Fig. 11, 1 km away from the northern (left-hand panel) or southern (right-hand panel) edge, computed for the 2D-smooth case by three teams using (a–b) FDM-S, (c–d) FPSM, (e–f) FDM-C. The SEM2-BE solution is taken as a reference and is plotted in black. The level of agreement between each solution and the reference is quantified by the time-frequency goodness-of-fit (GOF) in amplitude (top panel) and phase (bottom panel). The colour scale indicates the level of GOF, from 7 to 10 (perfect fit). The average GOF is indicated on top of the time-frequency subplots.

which provides an a posteriori justification for considering the latter a reference.

The out-of-plane component (which mainly consists of *SH* and Love waves) computed by FDM-S, FDM-C, FPSM and SEM1-BE at the northern and southern receivers are shown in Figs S1 and S2, respectively, and the FDM-S solutions computed with different grid spacings and implementations of the effective medium are shown in Fig. S3. The same conclusions as for the in-plane component can be drawn and are thus not repeated here.

6.2 2-D valley with gradient in sediments

Given the considerable cost to compute the solution of the 2D-sharp case with SEM2-F, we consider instead the SEM2-BE solution computed with the BE strategy as a reference. The seismograms of the horizontal ground velocity, computed with SEM2-BE along the two surface profiles of Fig. 11, are shown in Fig. 26. As for the 2D-sharp case, we observe a strong asymmetry in the spontaneous generation of surfaces waves following the slope of the valley edge. Note also that the surface waves, in particular Love waves, are less dispersed than in the 2D-sharp case (compare with Fig. 22), as expected from the analysis of the 1D-sharp and 1D-smooth solutions (Figs 8 and 10).

Fig. 27 shows the horizontal component of the in-plane component of the ground velocity computed at the northern and southern receivers by FDM-S, FDM-C and FPSM, and their comparison with the reference SEM2-BE solution. Note the excellent level of agreement in the early part of the signals, including the Rayleigh waves recorded at the northern receiver, and the overall good fit obtained for the late Rayleigh waves (generated at the northern valley edge) at the southern receiver.

The effect of varying the grid resolution and the definition of the effective medium in the FDM-S solution is shown in Fig. S4. Consistently with the analysis of the 1D-smooth results, we observe only a slight increase of GOF with respect to the SEM2-BE solution when switching from the isotropic to the orthorhombic effective medium, the accuracy being mainly controlled by the spatial resolution of the grid. Note also that the SEM2-BE solution, although not optimal, can be reasonably considered a reference. The tiny remaining difference between the 5 m orthorhombic FDM-S solution and the SEM2-BE solution can be partly attributed to the fact that the latter is not exact.

For the sake of completeness, we show in Fig. S5 the comparison of the horizontal out-of-plane component at the northern and southern receivers. Similar conclusions can be drawn as for the in-plane component: the overall level of agreement between solutions is very good, even for some of the late Love wave arrivals. Finally, in Fig. S6 we compare the predictions by FDM-S at the southern receiver for different grid spacings and definitions of the effective medium. We conclude again that due to the smoothness of the velocity model, the solution for the orthorhombic effective medium only slightly differs from that obtained using the harmonic averaging of moduli.

7 CONCLUSION

In order to better understand the origin of differences between 3-D numerical predictions of earthquake ground motion in realistic models of the Mygdonian basin, we have designed four canonical models and have compared several numerical solutions of the four cases for frequencies up to 4 Hz. The solutions were computed with the FPSM, the Legendre SEM and two formulations of the finite-difference method (FDM-S and FDM-C).

The comparisons show that both the accuracy of individual solutions and level of agreement between solutions vary with the type of seismic waves and depend on the smoothness of the velocity model. The level of accuracy is high for the body waves in the numerical solutions for all the models considered, whereas it systematically decreases in the sharp models for the surface waves. This is also observed for the realistic models of the Mygdonian basin (Maufroy *et al.* 2014).

The accuracy of the numerical solutions for the sharp models is shown to depend strongly on the discrete representation of the material interfaces (at which material parameters change discontinuously) inside the sediments. We have illustrated the dual nature of the implementation of interfaces in SEM: solutions computed with a mesh of elements whose boundaries follow the interfaces (F strategy) are optimally accurate, whereas solutions computed by approximating the discontinuities with the polynomial basis local to the elements can be extremely inaccurate for surface waves propagating along the interfaces. For all the numerical methods considered, except SEM if the F strategy can be applied, a proper implementation of interfaces requires the definition of an effective medium consistent with the interface boundary conditions. We have tested the efficiency of two explicit effective media: the isotropic volume harmonic and arithmetic averaging of elastic moduli and densities, respectively (Moczo *et al.* 2002), and its generalization to an orthorhombic effective medium (Moczo *et al.* 2014). Our results show that using the isotropic effective medium yields numerical solutions of limited accuracy for surface waves. They also indicate that reaching an acceptable accuracy by solely decreasing the size of the numerical grid may be extremely computationally expensive. Using instead the orthorhombic effective medium is shown to significantly improve the accuracy of the solutions and to preserve the computational efficiency of the methods.

The conclusions drawn from the analysis of the results of the canonical cases greatly help to explain the origin of the differences between numerical predictions of ground motion in realistic models of the Mygdonian basin (Maufroy *et al.* 2014). The persistent misfit between even the most similar solutions can be fairly attributed to the differences in the discrete representation of the material interfaces in sediments: The SEM solution was computed following the best-effort strategy in which the element boundaries do not follow the interfaces for depths smaller than a threshold value (the choice of which is the result of a compromise between accuracy and computational efficiency); the FDM-S and FPSM solutions used an isotropic effective medium with insufficiently small grid spacing (10 m for FDM-S and 7 m for FPSM, respectively).

These results have important implications regarding the accuracy of numerical prediction of earthquake ground motion in sedimentary basins, in particular with respect to local surface waves which play a critical role in the lengthening of ground motion duration and local amplifications at the basins' edges (e.g. Kawase 1996; Hallier *et al.* 2008). An improper discrete representation of the interfaces can cause considerably inaccurate numerical modelling of surface waves. Therefore, preparation of the computational model needs special care in this respect. Homogeneous layers within sediments should not be artificially introduced.

Whenever small-scale, or localized, strong variations of the material parameters have to be considered in the sediments, for example based on firm geological, geotechnical or geophysical evidence, an effective medium relevant for the chosen frequency range should be used. Depending on the degree of knowledge of the model heterogeneity and on the desired level of accuracy of the predictions, the effective media can be defined by procedures of increasing complexity. In the common situation where the level of uncertainty in the model (including the presence of interfaces) is large, a simple volume arithmetic average of the densities and slownesses, or a volume arithmetic average of the densities and harmonic average of the elastic moduli, should be used to provide an isotropic effective medium ready for numerical simulations. In all other situations, an upscaling procedure should be adopted to design an anisotropic effective medium, either by solving a homogenization problem as suggested by Guillot *et al.* (2010) and Capdeville *et al.* (2010b), or by following the explicit approach proposed by Moczo *et al.* (2014) based on the orthorhombic averaging.

Finally, our results confirm that there is no single numerical-modelling method that can be considered the best—in terms of accuracy and computational efficiency—for all structure-wavefield configurations. We recommend that any numerical method and code that is intended to be applied for numerical prediction of earthquake ground motion should be verified through stringent models that would make it possible to test the most important aspects of accuracy. We believe that the canonical cases presented in this paper, and made freely available to the seismological community (`http://www.sismowine.org`, last accessed 16 January 2015), can serve this purpose.

ACKNOWLEDGEMENTS

The authors are grateful to all the participants of E2VP and to Y. Capdeville for fruitful discussions about homogenization. F. de Martin thanks P. Thierry (Intel) for allowing access to the latest Sandy Bridge processors. The careful reading of the manuscript by one reviewer was very much appreciated.

The research presented in this paper was supported by the following projects or funding agencies: Cashima, Sigma, Stefanik, BRGM, MYGDONEMOTION APVV-0271-11 funded by the Slovak grant agency APVV, National Natural Science Foundation of China (Nos. 41090293, 41274053).

The SEM calculations were performed using the resources of the BRGM, of the CIMENT infrastructure (https://ciment.ujf-grenoble.fr, last accessed 16 January 2015) and of the CEA TGCC center acquired in the GENCI projects t2011046060, t2012046060 and t2013046060. The SEM meshes were designed using the commercial software Cubit (https://cubit.sandia.gov/, last accessed 16 January 2015). The FPSM calculations used the computational resources of CINECA—Consorzio Interuniversitario per il Calcolo Automatico (Bologna, Italy). Part of the FDM-S calculations were performed in the Computing Centre of the Slovak Academy of Sciences using the supercomputing infrastructure acquired in project ITMS 26230120002 and 26210120002 (Slovak infrastructure for high-performance computing) supported by the Research & Development Operational Programme funded by the ERDF.

REFERENCES

Backus, G.E., 1962. Long-wave elastic anisotropy produced by horizontal layering, *J. geophys. Res.,* **67**(11), 4427–4440.

Bard, P.-Y., 1994. Discussion session: lessons, issues, needs and prospects. Special Theme session 5: Turkey Flat and Ashigara Valley experiments, in *Proceedings of the Tenth World Conference of Earthquake Engineering,* Madrid, 19–24 July 1992, Vol. 11, pp. 6985–6988.

Bielak, J. *et al.*, 2010. The ShakeOut earthquake scenario: verification of three simulation sets, *Geophys. J. Int.,* **180**(1), 375–404.

Bouchon, M., 1981. A simple method to calculate Green's functions for elastic layered media, *Bull. seism. Soc. Am.,* **71**(4), 959–971.

Bouchon, M., 2003. A review of the discrete wavenumber method, *Pure appl. Geophys.,* **160**(3–4), 445–465.

Boyd, J.P., 2001. *Chebyshev and Fourier Spectral Methods,* Courier Dover Publications.

Capdeville, Y. & Marigo, J.-J., 2008. Shallow layer correction for spectral element like methods, *Geophys. J. Int.,* **172**(3), 1135–1150.

Capdeville, Y., Guillot, L. & Marigo, J.-J., 2010a. 1-D non-periodic homogenization for the seismic wave equation, *Geophys. J. Int.,* **181**(2), 897–910.

Capdeville, Y., Guillot, L. & Marigo, J.-J., 2010b. 2-D non-periodic homogenization to upscale elastic media for P–SV waves, *Geophys. J. Int.,* **182**(2), 903–922.

Chaljub, E., Cornou, C. & Bard, P.-Y., 2006. Numerical benchmark of 3D ground motion simulation in the valley of Grenoble, French Alps, in *Proceedings of the Third International Symposium on the Effects of Surface Geology on Seismic Motion,* LCPC edn, Vol. 2, pp. 1365–1375.

Chaljub, E., Komatitsch, D., Vilotte, J.-P., Capdeville, Y., Valette, B. & Festa, G., 2007. Spectral element analysis in seismology, in *Advances in Wave Propagation in Heterogeneous Media,* Vol. 48, Advances in Geophysics Series, pp. 365–419, eds WU, R.-S. & Maupin, V., Elsevier.

Chaljub, E., Moczo, P., Tsuno, S., Bard, P.-Y., Kristek, J., Kaser, M., Stupazzini, M. & Kristekova, M., 2010. Quantitative comparison of four numerical predictions of 3D ground motion in the Grenoble valley, France, *Bull. seism. Soc. Am.,* **100**(4), 1427–1455.

Coutant, O., 1989. *Program of numerical simulation AXITRA, Tech. rep.,* LGIT, Université Joseph Fourier, Grenoble, in French.

Cramer, C.H., 1995. Weak-motion observations and modeling for the Turkey Flat, U.S., Site-Effects Test Area near Parkfield, California, *Bull. seism. Soc. Am.,* **85**(2), 440–451.

Day, S.M., Bielak, J., Dreger, D., Graves, R., Larsen, S., Olsen, K.B. & Pitarka, A., 2001. *Tests of 3D elastodynamic codes: final report for lifelines project 1a01, Tech. rep.,* Pacific Earthquake Engineering Research Center & Southern California Earthquake Center.

Day, S.M., Bielak, J., Dreger, D., Graves, R., Larsen, S., Olsen, K.B. & Pitarka, A., 2003. *Tests of 3D elastodynamic codes: final report for lifelines project 1a02, Tech. rep.,* Pacific Earthquake Engineering Research Center.

Day, S.M., Bielak, J., Dreger, D., Graves, R., Larsen, S., Olsen, K.B. & Pitarka, A., 2005. *3D ground motion simulation in basins: final report for lifelines project 1a03, Tech. rep.,* Pacific Earthquake Engineering Research Center.

De Martin, F., 2011. Verification of a spectral-element method code for the Southern California Earthquake Center LOH.3 viscoelastic case, *Bull. seism. Soc. Am.,* **101**(6), 2855–2865.

Faccioli, E., Maggio, F., Paolucci, R. & Quarteroni, A., 1997. 2D and 3D elastic wave propagation by a pseudo-spectral domain decomposition method, *J. Seismol.,* **1**(3), 237–251.

Fichtner, A. & Igel, H., 2008. Efficient numerical surface wave propagation through the optimization of discrete crustal modelsa technique based on non-linear dispersion curve matching (DCM), *Geophys. J. Int.,* **173**(2), 519–533.

Fornberg, B., 1987. The pseudo-spectral method: comparisons with finite differences for the elastic wave equation, *Geophysics,* **52**(4), 483–501.

Guillot, L., Capdeville, Y. & Marigo, J.-J., 2010. 2-D non-periodic homogenization of the elastic wave equation: SH case, *Geophys. J. Int.,* **182**(3), 1438–1454.

Hallier, S., Chaljub, E., Bouchon, M. & Sekiguchi, H., 2008. Revisiting the basin-edge effect at Kobe during the 1995 Hyogo-Ken Nanbu earthquake, *Pure. appl. Geophys.,* **165**, 1751–1760.

Hisada, Y., 1995. An efficient method for computing Green's functions for a layered half-space with sources and receivers at close depths (part 2), *Bull. seism. Soc. Am.,* **85**(4), 1080–1093.

Hixon, R., 1998. Evaluation of a high-accuracy MacCormack-type scheme using benchmark problems, *J. Comput. Acoust.,* **6**(03), 291–305.

Kawase, H., 1996. The cause of the damage belt in Kobe: "the basin-edge effect," constructive interference of the direct *S*-wave with the basin-induced diffracted/Rayleigh waves, *Seism. Res. Lett.,* **67**(5), 25–34.

Kawase, H. & Iwata, T., 1998. A report on submitted results of the simultaneous simulation for Kobe, in *The Effects of Surface Geology on Seismic Motion, Recent Progress and new Horizon on ESG Study,* Vol. 3, eds Irikura, K., Kudo, K., Okada, H. & Sasatani, T., Balkema/CRC Press.

Klin, P., Priolo, E. & Seriani, G., 2010. Numerical simulation of seismic wave propagation in realistic 3-D geo-models with a Fourier pseudo-spectral method, *Geophys. J. Int.,* **183**(2), 905–922.

Komatitsch, D. & Martin, R., 2007. An unsplit convolutional perfectly matched layer improved at grazing incidence for the seismic wave equation, *Geophysics,* **72**(5), SM155–SM167.

Komatitsch, D. & Vilotte, J.P., 1998. The spectral-element method: an efficient tool to simulate the seismic response of 2D and 3D geological structures, *Bull. seism. Soc. Am.,* **88**(2), 368–392.

Komatitsch, D., Tsuboi, S. & Tromp, J., 2005. The spectral-element method in seismology, in *Seismic Earth: Array Analysis of Broadband Seismograms, Vol. 157 of Geophysical Monograph,* pp. 205–228, eds Levander, A. & Nolet, G., American Geophysical Union.

Kristek, J., Moczo, P. & Archuleta, R.J., 2002. Efficient methods to simulate planar free surface in the 3D 4th-order staggered-grid finite-difference schemes, *Stud. Geophys. Geod.,* **46**(2), 355–381.

Kristek, J., Moczo, P. & Galis, M., 2010. Stable discontinuous staggered grid in the finite-difference modelling of seismic motion, *Geophys. J. Int.,* **183**(3), 1401–1407.

Kristeková, M., Kristek, J. & Moczo, P., 2009. Time-frequency misfit and goodness-of-fit criteria for quantitative comparison of time signals, *Geophys. J. Int.,* **178**(2), 813–825.

Madariaga, R., 1976. Dynamics of an expanding circular fault, *Bull. seism. Soc. Am.,* **66**(3), 639–666.

Manakou, M., 2007. Contribution to the determination of a 3D soil model for site response analysis. The case of the Mygdonian basin, *PhD thesis*, (in Greek with English abstract), Department of Civil Engineering, Aristotle University of Thessaloniki.

Manakou, M.V., Raptakis, D.G., Chvez-Garca, F.J., Apostolidis, P.I. & Pitilakis, K.D., 2010. 3D soil structure of the Mygdonian basin for site response analysis, *Soil. Dyn. Earthq. Eng.,* **30**(11), 1198–1211.

Maufroy, E. *et al.*, 2014. Earthquake ground motion in the Mygdonian basin, Greece: the E2VP verification and validation of 3D numerical simulations up to 4 Hz, *Bull. seism. Soc. Am.,* in press.

Moczo, P., Kristek, J., Vavryčuk, V., Archuleta, R.J. & Halada, L., 2002. 3D heterogeneous staggered-grid finite-difference modeling of seismic motion with volume harmonic and arithmetic averaging of elastic moduli and densities, *Bull. seism. Soc. Am.,* **92**(8), 3042–3066.

Moczo, P., Kristek, J. & Gális, M., 2004. Simulation of the planar free surface with near-surface lateral discontinuities in the finite-difference modeling of seismic motion, *Bull. seism. Soc. Am.,* **94**(2), 760–768.

Moczo, P., Kristek, J. & Gális, M., 2014. *The Finite-Difference Modelling of Earthquake Motions Waves and Ruptures,* Cambridge Univ. Press.

Őzdenvar, T. & McMechan, G.A., 1996. Causes and reduction of numerical artifacts in pseudo-spectral wavefield extrapolation, *Geophys. J. Int.,* **126,** 819–828.

Peter, D. *et al.*, 2011. Forward and adjoint simulations of seismic wave propagation on fully unstructured hexahedral meshes, *Geophys. J. Int.,* **186**(2), 721–739.

Priolo, E., Carcione, J.M. & Seriani, G., 1994. Numerical simulation of interface waves by high-order spectral modeling techniques, *J. acoust. Soc. Am.,* **95**(2), 681–693.

Seriani, G. & Priolo, E., 1994. A spectral element method for acoustic wave simulation in heterogeneous media, *Finite Elem. Anal. Des.,* **16,** 337–348.

Soufleris, C., Jackson, J.A., King, G. C.P., Spencer, C.A. & Scholz, C.H., 1982. The 1978 earthquake sequence near Thessaloniki (northern Greece), *Geophys. J. Int.,* **68**(2), 429–458.

Stacey, R., 1988. Improved transparent boundary formulations for the elastic-wave equation, *Bull. seism. Soc. Am.,* **78**(6), 2089–2097.

Tam, C.K.W. & Webb, J.C., 1993. Dispersion-relation-preserving finite difference schemes for computational acoustics, *J. Comput. Phys.,* **107**(2), 262–281.

Theodulidis, N., Roumelioti, Z., Panou, A., Savvaidis, A., Kiratzi, A., Grigoriadis, V., Dimitriu, P. & Chatzigogos, T., 2006. Retrospective prediction of macroseismic intensities using strong ground motion simulation: the case of the 1978 Thessaloniki (Greece) earthquake (M6.5), *Bull. Earthq. Eng.,* **4**(2), 101–130.

Virieux, J., 1984. SH-wave propagation in heterogeneous media: Velocity-stress finite-difference method, *Geophysics,* **49**(11), 1933–1942.

Virieux, J., 1986. P-SV wave propagation in heterogeneous media: velocity-stress finite-difference method, *Geophysics,* **51**(4), 889–901.

Zhang, W. & Chen, X., 2006. Traction image method for irregular free surface boundaries in finite difference seismic wave simulation, *Geophys. J. Int.,* **167**(1), 337–353.

Zhang, W. & Shen, Y., 2010. Unsplit complex frequency-shifted pml implementation using auxiliary differential equations for seismic wave modeling, *Geophysics,* **75**(4), T141–T154.

Zhang, W., Zhang, Z. & Chen, X., 2012. Three-dimensional elastic wave numerical modelling in the presence of surface topography by a collocated-grid finite-difference method on curvilinear grids, *Geophys. J. Int.,* **190**(1), 358–378.

Zhang, Z., Zhang, W. & Chen, X., 2014. Complex frequency-shifted multi-axial perfectly matched layer for elastic wave modelling on curvilinear grids, *Geophys. J. Int.,* **198**(1), 140–153.

SUPPORTING INFORMATION

Additional Supporting Information may be found in the online version of this article:

Figure S1. East–west component of ground velocity at a receiver along the eastern surface profile of Fig. 11, 1 km away from the northern edge, computed for the 2D-sharp case by (a) FDM-S, (b) FPSM, (c) FDM-C, (d) SEM1-BE. The SEM2-F solution is taken as a reference and is plotted in black. The level of agreement between each solution and the reference is quantified by the time-frequency goodness-of-fit (GOF) in amplitude (top panel) and phase (bottom panel). The colour scale indicates the level of GOF, from 7 to 10 (perfect fit). The average GOF is indicated on top of the time-frequency subplots.

Figure S2. Same as Fig. S1 at a receiver 1 km away from the southern edge of the basin.

Figure S3. Same as Fig. S2 for solutions computed with FDM-S using different grid spacings and definitions of the effective medium: (a) harmonic averaging, 10 m; (b) harmonic averaging, 5 m; (c) orthorhombic averaging, 10 m; (d) orthorhombic averaging, 5 m.

Figure S4. North–south component of ground velocity at the southern receiver for solutions computed with FDM-S using different grid spacings and definitions of the effective medium: (a) harmonic averaging, 10 m; (b) harmonic averaging, 5 m; (c) orthorhombic averaging, 10 m; (d) orthorhombic averaging, 5 m. The level of agreement between each solution and the reference is quantified by the time-frequency goodness-of-fit (GOF) in amplitude (top panel) and phase (bottom panel). The colour scale indicates the level of GOF, from 7 to 10 (perfect fit). The average GOF is indicated on top of the time-frequency subplots.

Figure S5. Same as Fig. 27 for the east–west component of ground velocity at receivers along the eastern surface profile of Fig. 11, 1 km away from the northern (left-hand panel) or southern (right-hand panel) edge.

Figure S6. Same as Fig. S4 for the east–west component of ground velocity at the southern receiver. (http://gji.oxfordjournals.org/lookup/suppl/doi:10.1093/gji/ggu472/-/DC1).